nature cell biology

RESOURCE

Systematic genetic interaction screens uncover cell polarity regulators and functional redundancy

Bruno Thomas Fievet[1,5], Josana Rodriguez[1,5], Sundar Naganathan[2], Christine Lee[1], Eva Zeiser[1], Takao Ishidate[3], Masaki Shirayama[3], Stephan Grill[2,4] and Julie Ahringer[1,6]

Although single-gene loss-of-function analyses can identify components of particular processes, important molecules are missed owing to the robustness of biological systems. Here we show that large-scale RNAi screening for suppression interactions with functionally related mutants greatly expands the repertoire of genes known to act in a shared process and reveals a new layer of functional relationships. We performed RNAi screens for 17 *Caenorhabditis elegans* cell polarity mutants, generating the most comprehensive polarity network in a metazoan, connecting 184 genes. Of these, 72% were not previously linked to cell polarity and 80% have human homologues. We experimentally confirmed functional roles predicted by the network and characterized through biophysical analyses eight myosin regulators. In addition, we discovered functional redundancy between two unknown polarity genes. Similar systematic genetic interaction screens for other biological processes will help uncover the inventory of relevant genes and their patterns of interactions.

A major challenge in the study of developmental processes is the identification of all of the relevant genes and their functional relationships. Single-gene knockdown/knockout analyses have assigned gene functions on a large scale but owing to functional redundancy the single-gene approach cannot result in complete maps of developmental processes.

Genetic interaction screens have been extremely powerful for identifying genes whose products are functionally related in a direct or indirect manner[1–3]. In yeast, a genome-scale screen for synthetic interactions led to the first functional map of a eukaryotic cell[4]. However, generating comprehensive genetic interaction maps for individual developmental processes in an animal remains extremely challenging. One major difficulty is that the core components of biological processes are usually essential genes, making screening for genetic interactions difficult. In *C. elegans* and yeast the use of hypomorphic temperature-sensitive (*ts*) mutants can overcome this limitation[4–7]. We reasoned that applying RNA-mediated interference (RNAi) genetic interaction screening to a collection of functionally related *C. elegans* *ts* mutants focused on one developmental process would be a powerful approach for generating more comprehensive functional maps. We present here a metazoan cell polarity network derived from this strategy.

Cell polarity is important for the functions of most animal cells and its deregulation is implicated in disease[8]. Polarization is orchestrated by key conserved modules from worms to humans, such as the PAR proteins, and involves regulation of both the actomyosin and microtubule cytoskeletons. The first cell division of *C. elegans* is asymmetric and is an important model system for cell polarity studies[9,10]. Polarity is induced by redundant mechanisms and is dependent on the sperm centrosome and microtubules[11–15]. Consequently, during polarity establishment the cortical contractile actomyosin meshwork flows from posterior to anterior in a Rho-dependent manner[16–18], leading to an anterior localization of the PAR proteins PAR-3, PAR-6 and PKC-3 (atypical PKC) and posterior accumulation of PAR-1 and PAR-2 (refs 19–21). Subsequently, during polarity maintenance, anterior and posterior PAR proteins mutually antagonize each other, maintaining their asymmetric localizations[22]. The PAR proteins control downstream events such as the differential distribution of cell fate determinants and the posterior displacement of the mitotic spindle, the latter being regulated by a receptor-independent heterotrimeric G protein pathway[10].

Much of the above framework is derived from single-gene loss-of-function studies including RNAi phenotypic screens that identified genes with roles during the first cell division[23–25]. Despite these research efforts, the mechanisms of polarity induction and transduction are still unclear. The identification of missing genes and a wider network of interactions are required. Towards this goal, we have focused large-scale

[1]The Gurdon Institute and Department of Genetics, University of Cambridge, Cambridge CB2 1QN, UK. [2]Max Planck Institute of Molecular Cell Biology & Genetics, 01307 Dresden, Germany. [3]Program in Molecular Medicine, University of Massachusetts, Medical School, Worcester, Massachusetts 01605, USA. [4]Max Planck Institute for the Physics of Complex Systems, 01187 Dresden, Germany. [5]These authors contributed equally to this work.
[6]Correspondence should be addressed to J.A. (e-mail: j.ahringer@gurdon.cam.ac.uk)

Received 6 July 2012; accepted 2 November 2012; published online 16 December 2012; DOI: 10.1038/ncb2639

Table 1 Seventeen *ts* polarity mutants screened in this study.

Functional groups	Gene	*ts* allele	Description
Actomyosin regulation	*act-2*	*or621*	Actin
	let-502	*sb118*	Rho kinase/ROCK
	mel-11	*it26*	Myosin phosphatase
	nmy-2	*ne3409* *ne1490*	Non-muscle myosin heavy chain
PAR polarity	*par-1*	*zu310*	PAR-1/MARK kinase
	par-2	*it5*	RING-finger protein
	par-4	*it57* *it47*	LKB1/STK11 Serine/threonine kinase
	pkc-3	*ne4250* *ne4246*	Atypical protein kinase C
Spindle positioning and microtubule regulation	*gpa-16*	*it143*	G protein α
	let-99	*or204*	DEP domain protein
	lin-5	*ev571*	NUMA-related protein
	ric-8	*md303*	Gα GEF RIC8
	tbb-2	*qt1*	Tubulin
	zyg-9	*b244*	Microtubule regulator XMAP215/CKAP5

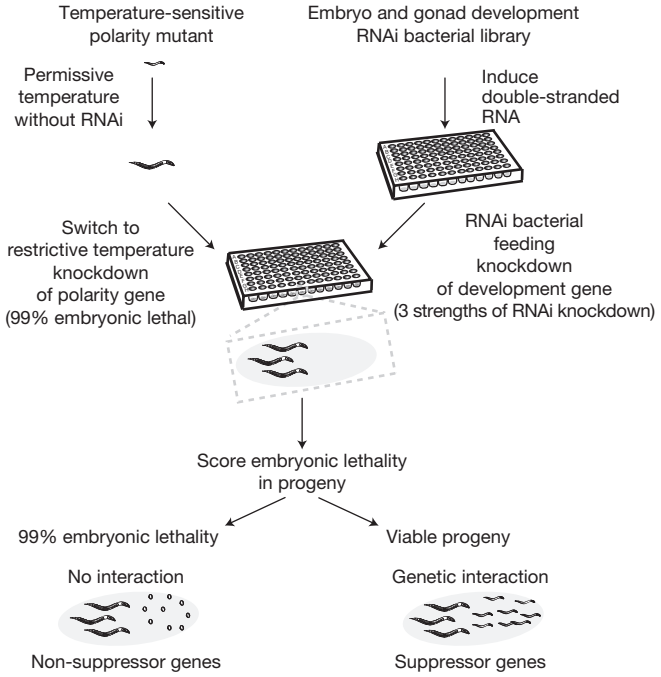

Figure 1 Suppressor genetic screen strategy. Flow chart describing the screening strategy followed to identify suppressors of polarity mutants. See Supplementary Fig. S1 and Tables S1–S3.

genetic suppressor screens on cell polarity, screening 2,745 genes by RNAi in 17 *ts* mutants of key cell polarity genes, generating a network of 184 genes. We demonstrate functional roles for new genes and uncover functional redundancy in early cell polarity. This network should be widely applicable across animals given the conservation of both the identified suppressors and cell polarity mechanism. Our screening approach will be valuable for creating functional maps of other biological processes.

RESULTS

The cell polarity network

To generate a cell polarity genetic network, we first selected 17 temperature-sensitive (*ts*) embryonic lethal mutants of 14 genes that function in one of three functional groups central to cell polarity: actomyosin regulation, PAR polarity and spindle positioning/microtubule regulation (Table 1). Each mutant was screened for suppression interactions, defined as rescue of embryonic lethality by RNAi depletion of a second gene (Fig. 1). Genetic suppression generally occurs between genes with opposing functions in a shared process. To allow the throughput necessary for screening a large number of mutants, we used an RNAi library likely to be enriched for relevant genes. Most known polarity genes are essential and we observed a fourfold enrichment of interactions between essential genes in a genome-wide *nmy-2(ts)* suppressor screen (data not shown). Therefore, we screened an RNAi sub-library targeting genes previously shown to have roles in embryo or germline development (~15% of the genome, see Methods and Supplementary Table S1). When both genes are essential, mutual suppression will in many cases require partial knockdown of each gene, as full inhibition will usually lead to strong lethality. Therefore, each *ts* mutant was screened at a temperature at which viability was around 1%, and each RNAi library clone was screened at three different strengths of RNAi knockdown (see Methods). We selected RNAi clones that have a reproducible suppressor activity and removed from our analysis genes likely to be nonspecific suppressors that can rescue many *ts* mutants independently of their biological function (see Methods and Supplementary Fig. S1 and Tables S2–S4). Connecting the suppressor genes to their 14 *ts* mutant seeds, we generated a cell polarity network containing 184 genes (nodes) and 227 genetic interactions (Fig. 2 and Supplementary Table S3).

Network captures expected interactions

To validate the network, we investigated whether we recovered known or expected interactions within each of the three functional groups. Myosin activity is tightly regulated by phosphorylation through the antagonistic activities of the myosin phosphatase *mel-11* (negative regulator) and the Rho kinase *let-502* (positive regulator)[26]. We found that *mel-11* and *let-502* are mutual suppressors, consistent with published data[26] (Fig. 2, PP1 box). As expected, RNAi of *mel-11* also suppresses the myosin mutant *nmy-2(ts)* and *nmy-2(RNAi)* suppresses the dominant actin allele *act-2(ts)* (ref. 27). Strikingly, genes coding for known actomyosin regulators (*unc-45*, *mlc-5* and *wip-1*), actin-binding proteins (*erm-1* and *pod-1*) and many small GTPases (*rga-3*, *arf-1.2*, *cdc-42* and *rab-7*) also fall within the actomyosin regulation group (Fig. 2, Actomyosin regulators and Small GTPase & regulators boxes).

An important aspect of polarity is the mutual antagonism between anterior and posterior PAR proteins[19,20]. Within the PAR polarity group, we found mutual suppression between all components of the anterior PAR complex and *par-2* as previously observed[5,20] (Fig. 2, Anterior PARs box). PAR proteins also control the timing of asymmetric cell division through the cell-cycle regulators polo kinase PLK-1 and CDC-25 (ref. 28). We observed that RNAi of *plk-1* or *cdc-25* suppresses *par-4(ts)* (Fig. 2, Other cell cycle regulators box). In mammals, LKB1/PAR-4 activity is regulated by binding to MO25 (ref. 29). RNAi of the MO25 homologue *mop-25.3* suppressed *par-4(ts)* (Fig. 2, LKB1 complex box), suggesting a conserved functional

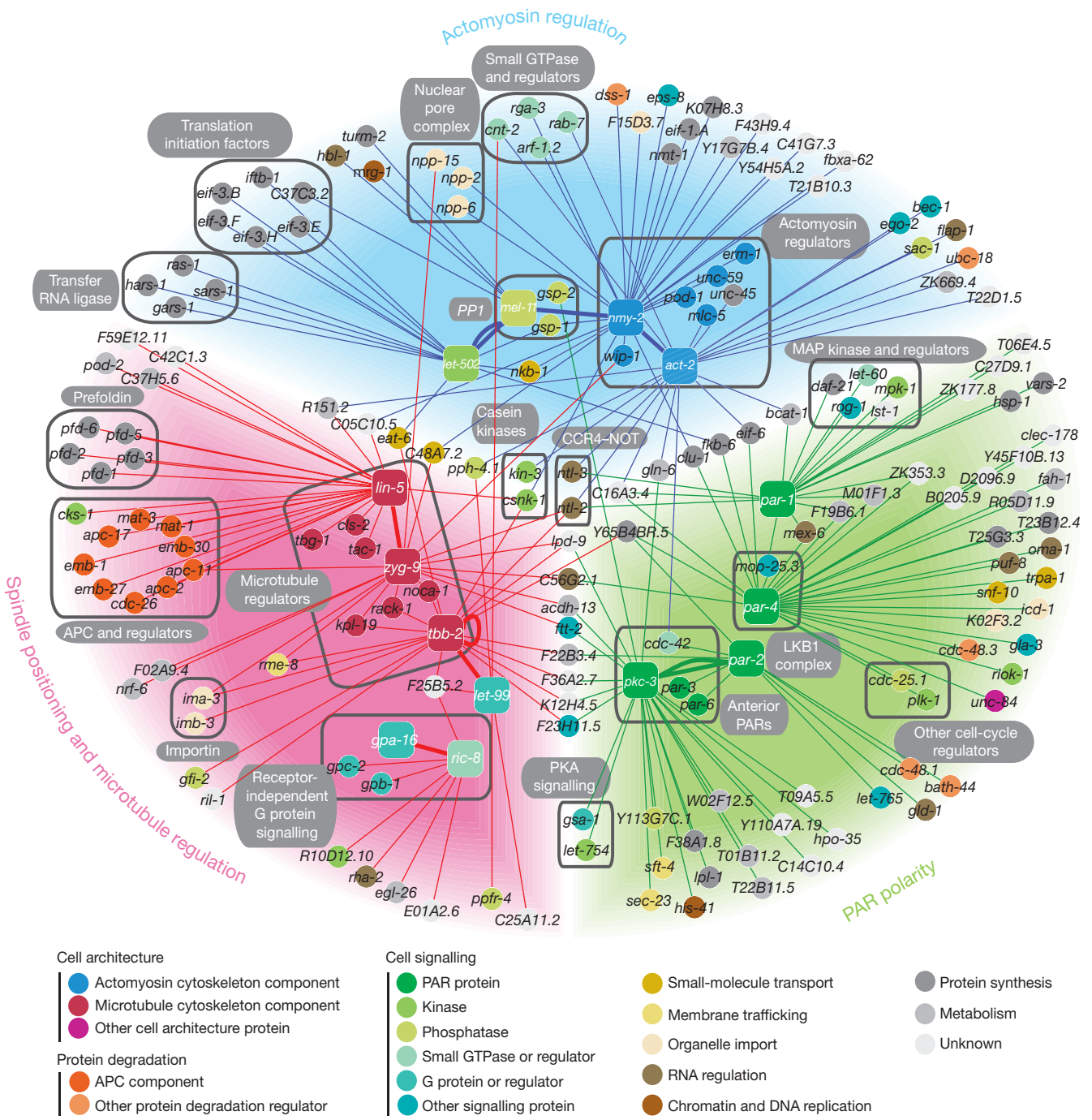

Figure 2 Cell polarity genetic network. Graphical network representation of 227 specific genetic interactions found between 184 genes. Coloured areas represent the three broad functional groups (Actomyosin regulation, blue; PAR polarity, green; Spindle positioning and microtubule regulation, red). Oblong nodes are the 14 *ts* polarity seeds screened and circular nodes are their suppressors. Lines represent the genetic interactions found and are coloured on the basis of the mutant functional group. Thick lines represent interactions found between seeds. Suppressors linked to only one seed are positioned in the outskirts of the network. Suppressors linking more than one seed are generally positioned between them. Nodes are colour-coded according to their functional class or sub-functional category. For representation purposes we only plotted genes from unique target RNAi clones. See Methods and Supplementary Tables S3 and S4.

link[30]. Asymmetric localization of cell fate determinants MEX-5/6 depends on a phosphorylation event requiring PAR-1 and PAR-4 activity[31]. Both *par-1(ts)* and *par-4(ts)* were rescued by *mex-6(RNAi)*, supporting the view that PAR-1 and PAR-4 negatively regulate MEX-6. We also detected the recently described genetic link between the Ras-MAP kinase pathway and *par-1* through *mpk-1*/MAPK and *let-60*/Ras (ref. 32). Strengthening this link, we further found that knockdown of three other MAP kinase regulators suppresses *par-1(ts)*: LST-1 (ref. 33), ROG-1 (ref. 34) and DAF-21 (ref. 35) (Fig. 2, MAP kinase and regulators box).

Forces positioning the spindle at the posterior involve a LIN-5, GPR-1/2 and Gα complex, together with dynein activity and the regulation of microtubule dynamics[10]. Within the spindle positioning/microtubule regulation group, we observed that LIN-5 is suppressed by many RNAi knockdowns that lead to shorter microtubules: *zyg-9*/XMAP215, *tac-1*/TACC, γ-tubulin, prefoldins (involved in tubulin folding) and the CLASP *cls-2* (Fig. 2, Microtubule regulators and Prefoldin boxes). This suggests that LIN-5 might increase spindle pulling forces through increased microtubule plus-end depolymerization. RIC-8 is a guanine nucleotide exchange factor that controls spindle pulling forces through G protein signalling[10]. We found that *ric-8(ts)* is suppressed by RNAi of heterotrimeric G protein subunit genes *gpa-16* (Gα), *gpb-1* (Gβ) and *gpc-2* (Gγ) (Fig. 2, Receptor-independent G protein signalling box). In addition, *let-99(RNAi)* suppressed the *tbb-2(ts)* gain-of-function mutant[36] (Fig. 2, Microtubule regulators box) supporting the proposal that the DEP domain protein LET-99 regulates microtubule dynamics[37].

The 26 genes connecting *ts* mutants from different functional groups are likely to integrate information between polarity processes. The small GTPase CDC-42 is a key conserved regulator of actin dynamics and functions with the anterior PAR complex[5]. We find that *cdc-42* connects the actomyosin and PAR polarity groups through *act-2* and *par-2* (Fig. 2, Anterior PARs box). The casein kinase I *csnk-1* connects the actomyosin regulation and spindle-positioning groups (Fig. 2; Casein kinases box). The excessive cortical activity and increased spindle pulling forces associated with *csnk-1* loss of function are compatible with this pattern of interaction[38]. Two highly connected genes are components of the multifunctional CCR4–NOT complex; *ntl-2* connects all three groups and *ntl-3* connects actomyosin regulation and PAR polarity groups (Fig. 2; CCR4–NOT box). The CCR4–NOT complex, through its multi-enzymatic activities, regulates gene expression at different levels, including transcriptional repression, messenger RNA decay and protein ubiquitylation[39]. The core component of this complex (NTL-1) controls spindle positioning in *C. elegans* asymmetric first cell division by regulating ZYG-9 protein levels[40]. The connectivity of *ntl-2* and *ntl-3* suggests that the CCR4–NOT complex might regulate the levels of multiple polarity regulators.

A new layer of functional interactions

To further evaluate the capacity of our network to identify relevant functional interactions, we focused on 37 well-characterized polarity genes with published data from single-gene studies. We built a high-confidence functional network containing 49 interactions between these 37 genes (Fig. 3a black lines and Supplementary Table S5) and used this network as a reference to evaluate the relevance of networks generated by our and other large-scale studies. Using published large-scale data derived from phenotypic profiling screens analysing the gonad structure and the embryonic first cell division, we obtained a network of 29 functional interactions for these 37 genes[25,35] (Fig. 3b grey and blue lines, respectively). In comparison, our suppressor screen found 21 interactions (Fig. 3b orange lines) out of which only three are in common with the phenotypic network, indicating that our suppressor screen is as informative as phenotypic screens to identify relevant functional relationships. Strikingly, the global architecture of the 47 interactions obtained by combining these two large-scale

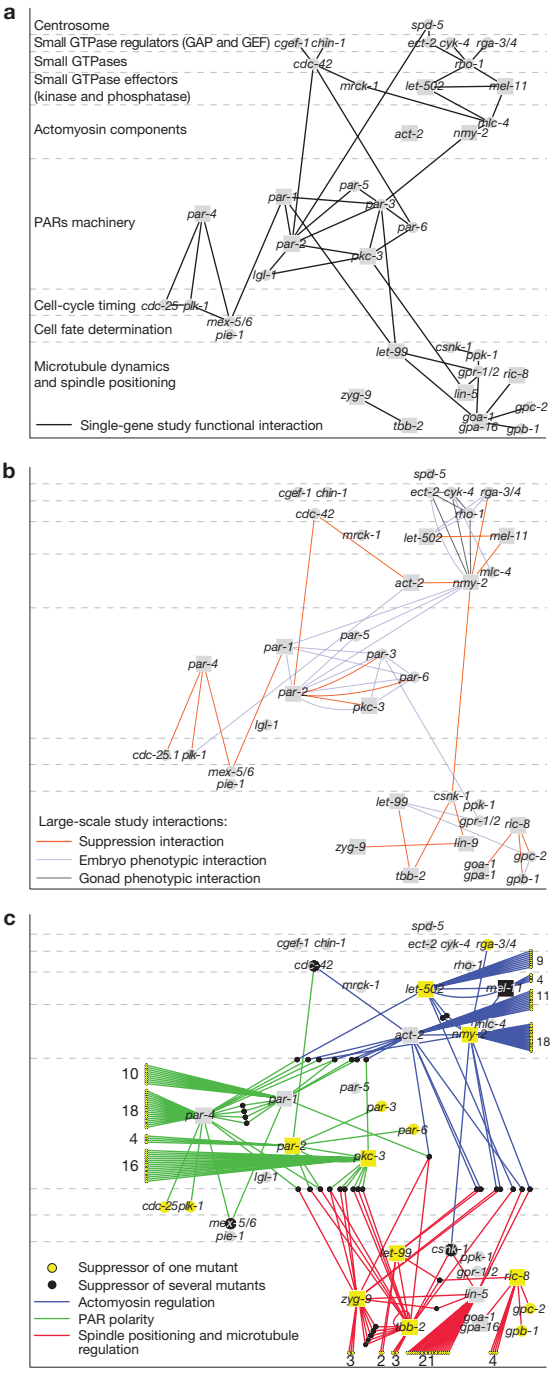

Figure 3 Suppressor screen identifies a new layer of functional relationships. (**a**) Network built from functional interactions found in single-gene studies between 37 well-characterized polarity genes. Nodes are positioned according to their molecular function (left labels) and square seeds are the 14 *ts* polarity genes screened. (**b**) Network built for the same 37 polarity genes based on interactions inferred from large-scale studies. Suppression interactions (orange lines, this study) show a complementary pattern to phenotypic interactions found in phenotypic analysis of embryo first cell division (blue lines)[25] and gonad structure (dark grey lines)[35]. (**c**) Network representing all of the interactions found in this study. One hundred and thirty-eight suppressors are connected to a single mutant (yellow nodes) and 41 have more than one connection (black nodes). Note that 9 out of 14 polarity seeds were also found as suppressors. When required, the number of interactions found for a mutant is indicated. Genetic interactions are coloured as in Fig. 2. See Supplementary Table S5.

data is similar to the 49 interactions of the single-gene study polarity network. Together, the two large-scale data sets complement each other and identify many of the cell polarity interactions reported from single-gene research. Adding the 160 suppressors reported here to the network of 37 known polarity genes greatly expands the collection of genes implicated in cell polarity (Fig. 3c). Importantly, 80% of the suppressors have a human homologue and 16% are completely uncharacterized (Supplementary Table S3).

Prediction of gene function and signalling crosstalk

We observed that some polarity mutants are suppressed by a set of genes that act together in a common cellular process, strongly implicating a functional link between them. For example, in the spindle positioning/microtubule regulation group, RNAi of 9 APC subunits (*apc-2*, *cdc-26*, *emb-27*, *emb-30*, *mat-1*, *mat-3*, *apc-11*, *emb-1* and *apc-17*) suppressed *lin-5(ts)*. To investigate whether other uncharacterized suppressors of *lin-5(ts)* could be regulators or unknown components of APC complex, we tested whether their knockdown enhanced lethality of the APC subunit mutant *mat-3(ts)*. We found that F59E12.11 enhanced *mat-3(ts)* embryonic lethality and caused a meiotic arrest phenotype characteristic of APC loss of function (data not shown). Supporting our hypothesis that F59E12.11 could be an APC subunit or regulator, it has recently been reported that RNAi knockdown of F59E12.11 causes a gonad defect similar to that of a group of proteins enriched for APC components[35]. F59E12.11 has an uncharacterized human homologue, LOH12CR1, which would be a promising candidate for future study.

Within the PAR polarity group, we found connections between two members of the protein kinase A (PKA) signalling pathway and *pkc-3(ts)*: *gsa-1* (Gαs) and *let-754* (adenylate kinase). As the PKA signalling pathway has not been reported to regulate PKC-3 in early embryo development, we explored this connection by testing 13 predicted members of the PKA pathway not screened, including positive and negative regulators (Fig. 4a). Strengthening this connection, we found that RNAi of two positive regulators of PKA signalling, *acy-3* and *let-607*, suppressed *pkc-3(ts)*, whereas RNAi of two negative regulators, *kin-2* and *pde-1*, enhanced *pkc-3(ts)* lethality. Knockdown of the Gα GEF *ric-8*, which genetically interacts with the PKA pathway during synaptic signalling[41], also enhanced *pkc-3(ts)* (Fig. 4). These results implicate a previously unknown negative crosstalk between the PKA signalling pathway and PKC-3 function.

Interaction patterns identify polarity regulators

Most genes in the network do not have a clear polarity role based on data from phenotype profiling screens (Supplementary Table S3)[23–25], suggesting that their loss-of-function phenotype is subtle or that functional redundancy might mask their polarity role. We reasoned that genes directly relevant to particular polarity functions would show opposite patterns of suppression and enhancement in backgrounds with opposing effects on the process. For example, the anterior PAR complex and posterior PAR-2 maintain their distinct domains through negative regulatory interactions; RNAi of anterior PAR genes *par-3* or *cdc-42* suppresses lethality of the posterior PAR mutant *par-2(ts)* (ref. 5; Fig. 2, Anterior PARs box) but enhances lethality of the anterior PAR mutant *pkc-3(ts)* (Fig. 5a).

Using this strategy, we found that RNAi of five new *par-2* suppressors enhanced lethality of *pkc-3(ts)* (Fig. 5a). We next tested whether the

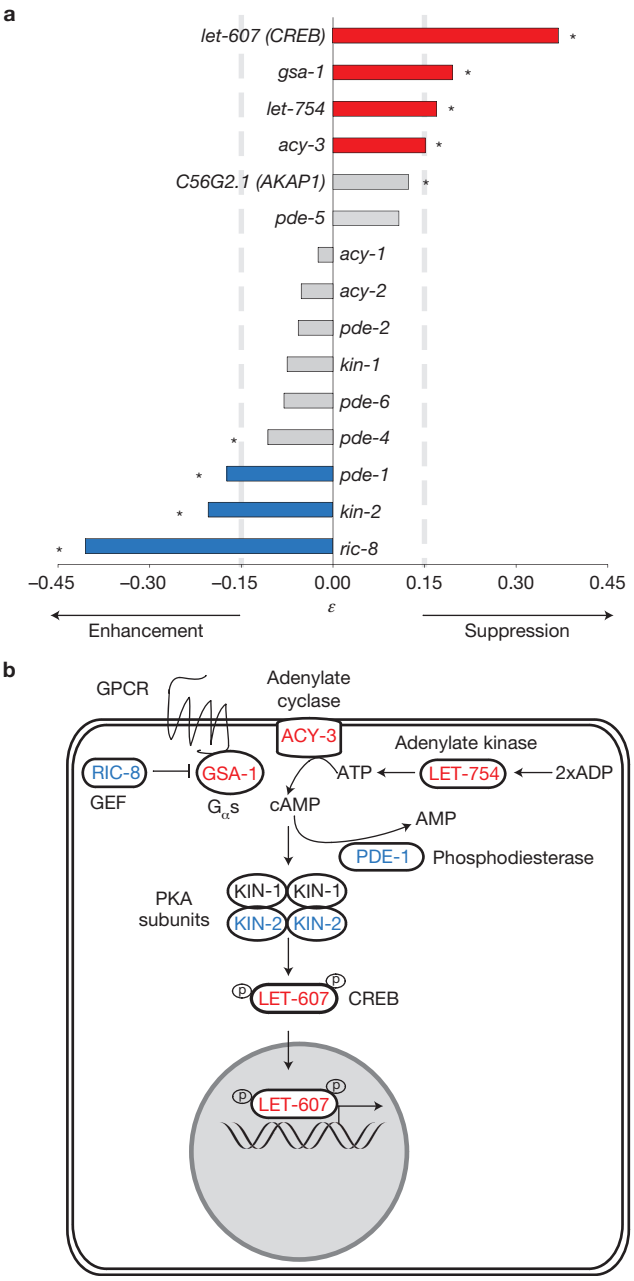

Figure 4 PKA signalling antagonizes PKC-3 function. (**a**) Bar graph representing the strength of the genetic interactions between *pkc-3(ts)* and genes from the PKA signalling pathway. ε represents the deviation of the observed double-knockdown fitness from expectation. A strong interaction is considered when $|\varepsilon| \leq 0.15$ (doted line) and *Z*-test $P < 0.001$ (*). PKA signalling components (*let-607*, *gsa-1*, *let-754* and *acy-3*) suppress the *pkc-3(ts)* mutant and PKA negative regulators (*pde-1*, *kin-2* and *ric-8*) enhance the *pkc-3(ts)* mutant. (**b**) Cellular schematic representation of the PKA signalling pathway indicating in red the suppressors and in blue the enhancers of *pkc-3(ts)*.

candidates showing *par-2* suppression and *pkc-3* enhancement have polarity roles. To sensitively identify defects, we carried out assays in the *pkc-3(ts)* background at the permissive temperature, where defects are negligible, quantifying PAR-2 localization, cell size asymmetry and the distribution of the cell fate determinant MEX-5. We found that RNAi

a

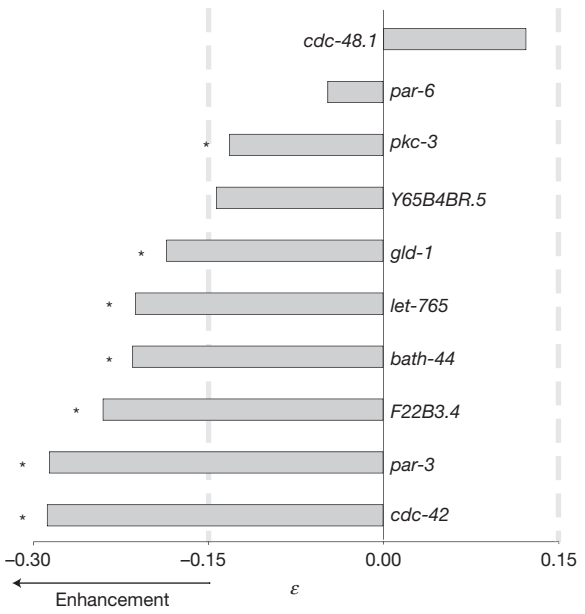

b

	Posterior PAR-2	Cell-size asymmetry	MEX-5 anterior enrichement
par-3	Altered	Altered	Altered
Y65B4BR.5	Altered	Altered	Altered
F22B3.4	Altered	Altered	Altered
bath-44	No defect	Altered	No defect
let-765	No defect	No defect	No defect

c

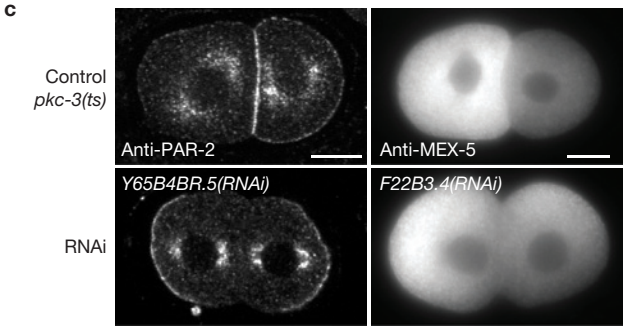

Figure 5 Characterization of new PAR protein regulators acting upstream and downstream of PARs. (**a**) Bar graph representing the strength of the genetic interactions between *par-2* suppressors in *pkc-3(ts)*. A strong interaction is defined as in Fig. 4. *par-6*(*RNAi*) and *pkc-3*(*RNAi*) induce strong embryonic lethality in the wild type, preventing the detection of strong enhancement. (**b**) Table summarizing polarity phenotypes observed in *pkc-3(ts)* after RNAi of strong enhancers. *gld-1*(*RNAi*) induces sterility preventing its phenotypic characterization. (**c**) Midsection of two-cell-stage *pkc-3(ts)* embryos stained for PAR-2 (left) and fluorescence micrographs of two-cell stage embryos stained for the cell fate determinant MEX-5 (right). Control images of *pkc-3(ts)* embryos at the permissive temperature (top row). Representative defective phenotypes observed after RNAi of *pkc-3(ts)* enhancers (bottom row). Scale bars, 10 μm. See Supplementary Fig. S2.

of *bath-44* affects cell size asymmetry and that Y65B4BR.5 and F22B3.4 affect all three aspects of polarity assayed (Fig. 5b,c and Supplementary Fig. S2). These results suggest that Y65B4BR.5 and F22B3.4 probably act upstream of PAR protein localization whereas *bath-44* functions downstream or in parallel to the PAR proteins. Homologues of these proteins are involved in protein folding (Y65B4BR.5/NACA), post-translational protein modification (F22B3.4/GFPT1) or protein degradation (BATH-44/SPOP), suggesting potentially complex regulation of PAR protein activity (Supplementary Fig. S3a).

To identify new actomyosin regulators we selected two mutants with opposite phenotypes: the *nmy-2* loss-of-function mutant leads to a loss of contractile activity[42], whereas the dominant allele of the actin gene *act-2* increases contractile activity dependent on myosin function[27]. Similar to the above analysis, we screened for RNAi suppressors of *nmy-2(ts)* that enhanced the lethality of *act-2(ts)* and vice versa. We found that 13 RNAi suppressors of *act-2(ts)* strongly enhanced the lethality of *nmy-2(ts)* (Fig. 6a), and 12 RNAi suppressors of *nmy-2(ts)* enhanced the lethality of *act-2(ts)* (Fig. 6b). Notably, of these 25 actomyosin suppressor/enhancer genes, four are known regulators of myosin function (*cdc-42*, *unc-45*, *nmy-2* and *mlc-5)* and four others have been shown to affect cortical dynamics (*rga-3*, *csnk-1*, *ntl-3* and *pod-1)*, suggesting that the remaining 17 genes are excellent candidates for regulating actomyosin function.

Biophysical analyses confirm new myosin regulators

Before polarity induction, the actomyosin cytoskeleton is organized in a dynamic meshwork of large interconnected foci all around the cortex. During polarity establishment, myosin foci move towards the anterior inducing a cortical flow that is dependent on the gradient of myosin contractility and the cortical viscosity[43]. To sensitively assess the involvement of *act-2* and *nmy-2* suppressors in actomyosin dynamics, we performed live-cell imaging of NMY-2::GFP (Supplementary Video S1) and measured three parameters that reflect myosin activity, cortex viscosity and myosin cortical distribution. First, to quantify myosin activity we measured NMY-2 cortical flow velocity at 30% retraction. Second, as a proxy of cortical viscosity we determined the range of flow (derived from the myosin localization profile and cortical flow velocity)[43]. Third, to evaluate myosin cortical distribution we calculated the coefficient of variation (c_v) of myosin intensity at the onset of flow (high if NMY-2 is restricted to foci and low if NMY-2 is homogeneously distributed).

To determine the sensitivity of these three parameters for identifying actomyosin regulators, we measured them in the wild type and after RNAi of five known actomyosin regulators (*cdc-42*, *csnk-1*, *mlc-5*, *rga-3* and *unc-45*). For each of these five genes, at least one of the parameters was significantly altered (Fig. 6c and Supplementary Figs S4, S5 and Videos S2–S5). We next tested four previously unknown *nmy-2* enhancers (*cnt-2*, *ntl-2*, *plst-1* and *sac-1*) and five new *act-2* enhancers (*erm-1*, *gsp-1*, *npp-2*, *unc-59* and Y54H5A.2). Of these nine genes, RNAi of eight significantly affected flow velocity (Y54H5A.2, *plst-1*, *unc-59*, *erm-1*, *cnt-2*, *gsp-1*; Supplementary Videos S6–S11), the range of flow (*ntl-2*, *npp-2* and *unc-59*) or the distribution of cortical myosin (*npp-2*, it unc-59, *gsp-1* and *erm-1*; Fig. 6c and Supplementary Figs S4 and S5).

Five of these genes (*erm-1*, *plst-1*, *unc-59*, *cnt-2* and *gsp-1*) have homologues functionally linked to the actin cytoskeleton in mammals (Supplementary Fig. S3b) and we now implicate them in the regulation of actomyosin dynamics at the cell cortex during polarity establishment. The nuclear pore protein NPP-2 (NUP85), the CCR4–NOT component NTL-2 (CNOT2) and the conserved uncharacterized Y54H5A.2 (FAM203A) have not previously been shown to regulate the actin cytoskeleton. Surprisingly, none of these

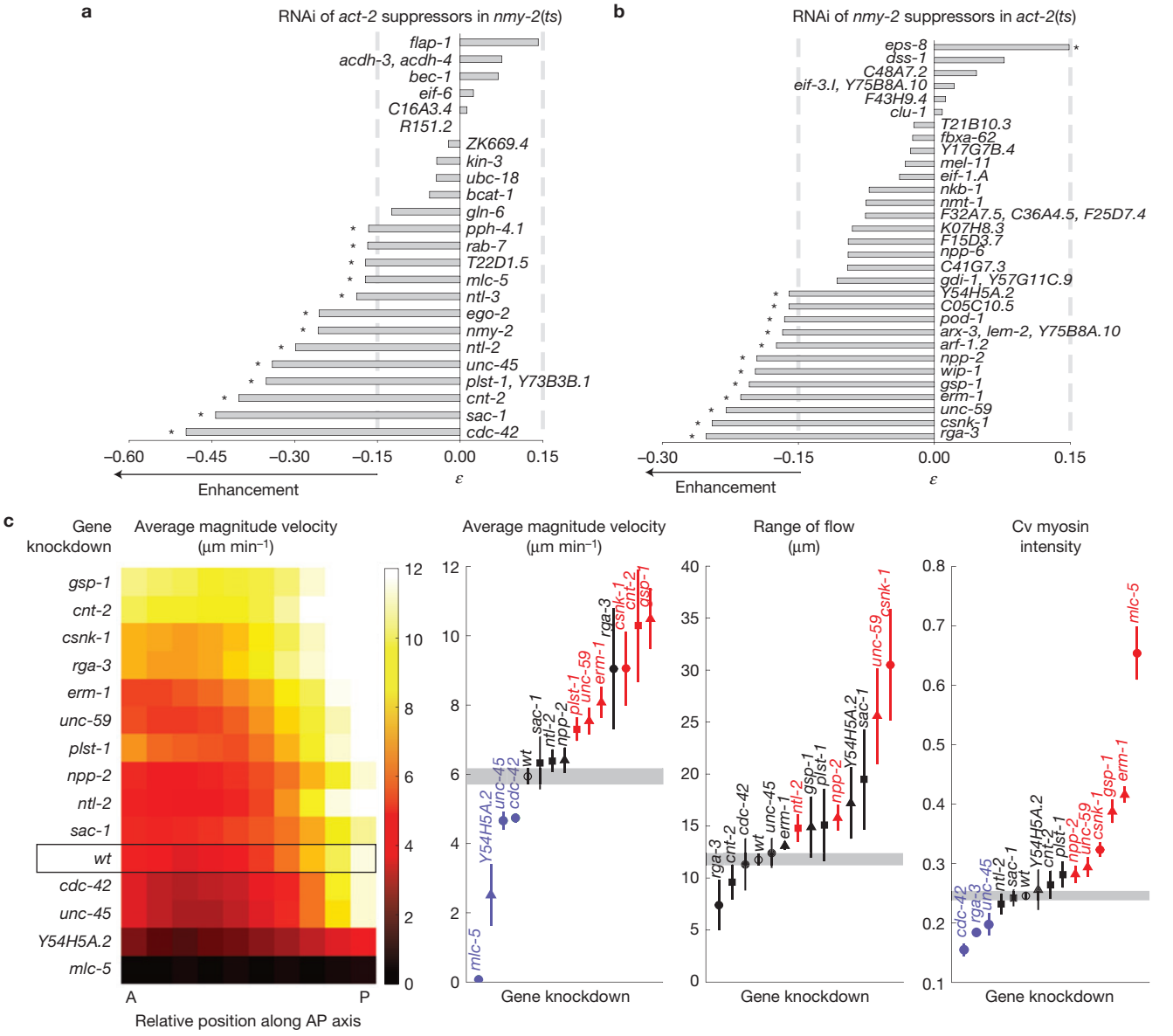

Figure 6 Biophysical characterization of new actomyosin regulators. (**a**,**b**) Bar graph representing the strength of the genetic interactions between *act-2* suppressors in *nmy-2(ts)* (**a**) and *nmy-2* suppressors in *act-2(ts)* (**b**). A strong interaction is defined as in Fig. 4. For this analysis we also included RNAi clones targeting multiple genes, which are not considered in Fig. 2. (**c**) New polarity candidates affect actomyosin functions important for anterior flow physical properties or cortical structure during polarity establishment. From left to right: map representing the magnitude velocity of NMY2::GFP along the anterior–posterior (AP) axis at 30% retraction for each gene knockdown; graphs representing respectively the average magnitude velocity in the whole embryo, the range of flow and the coefficient of variation (Cv) of myosin intensity, measured for all RNAi conditions. In all graphs, genes marked in red represent a significant increase and genes in blue a significant decrease (Welch *t*-test at 95% confidence). Error bars indicate s.e.m. Circles represent wild-type and known regulators, squares represent *nmy-2* enhancers and triangles represent *act-2* enhancers. See Supplementary Figs S4 and S5.

new regulators was found when assessed by RNAi knockdown and differential interference contrast (DIC) video-recording. These data demonstrate that the genetic interaction network combined with secondary suppressor/enhancer screening identifies relevant genes missed by other large-scale screening methods.

Functional redundancy in cell polarity

In the spindle positioning/microtubule regulation group, the most highly connected suppressor is *F25B5.2*, an uncharacterized gene. *F25B5.2(RNAi)* embryos show no contractile activity and no pseudocleavage furrow (Fig. 7a *F25B5.2(RNAi)*). Surprisingly, despite these strong cortical defects, *F25B5.2(RNAi)* embryos are viable. These phenotypes are very similar to those reported for the *nop-1(it142)* mutant, which genetically maps near F25B5.2 (Fig. 7a)[44]. We found that *nop-1(it142)* mutants have a stop codon in *F25B5.2* (Trp696Stp) and that a transgene encoding *F25B5.2* rescues the *nop-1* mutant phenotype (Fig. 7a). Therefore, *nop-1(it142)* is a loss-of-function allele of *F25B5.2* (renamed *nop-1*) . GFP::NOP-1 shows a dynamic localization, being present at the cortex during polarity establishment but not during polarity maintenance (Fig. 7b).

To characterize NOP-1 function in cell polarity, we examined the distributions of NMY-2 and PAR-3 in *nop-1* mutant embryos. NMY-2

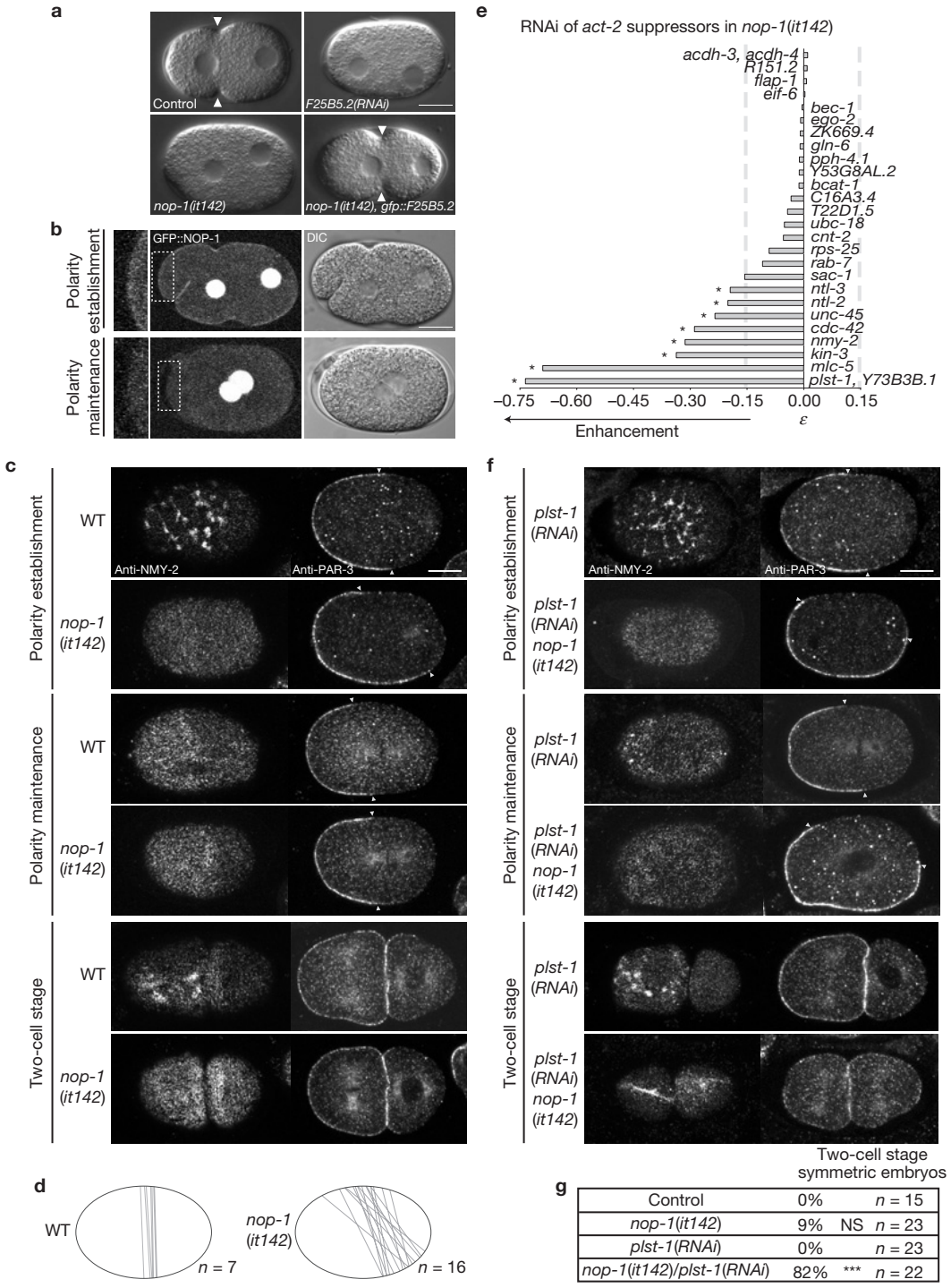

Control	0%		n = 15
nop-1(it142)	9%	NS	n = 23
plst-1(RNAi)	0%		n = 23
nop-1(it142)/plst-1(RNAi)	82%	***	n = 22

Figure 7 NOP-1 (F25B5.2) regulates actomyosin localization and dynamics, affects cell polarity establishment and acts redundantly with PLST-1 during polarity maintenance. (**a**) One-cell stage DIC images of control (wild type), *F25B5.2(RNAi)*, *nop-1(it142)* and *nop-1(it142);gfp::F25B5.2* embryos. Pseudo-cleavage can be observed during polarity establishment in control embryos (white arrowheads). *F25B5.2(RNAi)* and *nop-1(it142)* embryos do not show a pseudo-cleavage. Pseudo-cleavage formation is rescued in *nop-1(it142);gfp::F25B5.2* embryos. (**b**) Confocal (left) and DIC (right) images of one-cell stage *nop-1(it142);gfp::nop-1* life embryos. During polarity establishment GFP::NOP-1 is present at the cell cortex and its level decreases during polarity maintenance. The nuclear localization could be nonspecific because unfused GFP has been reported in the nucleoplasm but never at the cortex. (**c**,**f**) Projection of cortical sections of wild-type (WT) and *nop-1(it142)* embryos (**c**) or *plst-1(RNAi)* and *plst-1(RNAi)/nop-1(it-142)* embryos (**f**) stained for NMY-2 (left images) and midsection of embryos stained for PAR-3 (right images). Embryo stages are indicated on the left. Arrowheads indicate PAR-3 boundaries. (**d**) Embryo schematic illustrations representing PAR-3 front of retraction (grey line) during polarity establishment phase in 7 control versus 16 *nop-1(it142)* embryos. (**e**) Bar graph representing the strength of the genetic interactions between *act-2(ts)* suppressors in *nop-1(it142)*. A strong interaction is defined as in Fig. 4. (**g**) Table indicating the percentages of embryos in control (wild type), *nop-1(it142)*, *plst-1(RNAi)* or *plst-1(RNAi)/nop-1(it-142)* conditions showing a symmetric first cell division. $^{***}P < 0.001$ by Fisher's exact test; NS, not significant. Scale bars, 10 μm.

failed to form foci or to retract during polarity establishment (Fig. 7c and Supplementary Video S12), consistent with the previously reported failure to form an anterior actin cap[44]. Despite the lack of NMY-2 asymmetry during polarity establishment, we observed partial anterior enrichment of PAR-3 (Fig. 7c,d), suggesting that PAR-3 becomes asymmetric by an NMY-2-independent mechanism during polarity establishment in the *nop-1* mutant. Strikingly, NMY-2 and PAR-3 distribution defects are corrected at the polarity maintenance phase, and 98% of embryos are viable. We conclude that NOP-1 acts specifically during polarity establishment to regulate actomyosin function and that a functionally redundant mechanism acts during maintenance phase.

We reasoned that knocking down a functionally redundant gene in the viable *nop-1(it142)* mutant background would be expected to cause synthetic lethality and that suppressors of *act-2(ts)* would be good candidates, as they impair NMY-2 distribution or function. RNAi of eight suppressors of *act-2(ts)* genetically enhanced *nop-1(it142)* (Fig. 7e), with *plst-1* and *mlc-5* having the greatest effects. RNAi of *mlc-5* causes strong lethality due to cytokinesis[45] and polarity defects in a wild-type background. In contrast, RNAi of *plst-1* is not lethal in a wild-type background and shows a normal pattern of NMY-2 and PAR-3 localization (Fig. 7f). The polarity defects of *nop-1(it142); plst-1(RNAi)* embryos are similar to those in *nop-1(it142)* alone during polarity establishment (Fig. 7f). Remarkably, the NMY-2 localization and PAR-3 defects were not corrected, leading to total loss of polarity and a symmetric first cell division in 82% of embryos (Fig. 7f,g). Therefore, PLST-1 activity during polarity maintenance corrects the early polarity defects of *nop-1* mutants. These results demonstrate that NOP-1 and PLST-1 act in partially redundant pathways to ensure correct polarity establishment and maintenance through regulation of NMY-2 activity.

DISCUSSION

We present an approach for comprehensively building networks for individual biological processes by systematically focusing multiple high-throughput RNAi genetic interaction screens across different aspects of a given process. Using this approach, we generated a cell polarity network of 186 genes by screening mutants of 14 well-characterized polarity genes. This is a key step towards the task of identifying all of the genes in metazoans involved in cell polarity.

Our screening strategy using a sub-library of genes relevant to embryo development is highly efficient compared with a genome-wide approach. We tested a total of 47,000 potential suppression interactions with 14 polarity genes. Screening genome-wide, a similar number of interactions would identify suppressors for only two mutants, which would be insufficient to build a network. Published genome-wide screens for 2 of the mutants used in our study, *par-1(ts) and par-2(ts)*, identified a total of 14 suppressors using strong RNAi knockdown conditions[5,32]. Our screen could potentially have identified five of these suppressors and we detected two. In contrast, for these 2 mutants we identified 29 suppressors, of which 27 were not found in the genome-wide screens. Therefore, screening at three different strengths of RNAi is more sensitive for detecting genetic interactions between essential genes. For example, we found that RNAi of five components of the MAP signalling pathway suppressed *par-1(ts)*, whereas the published screen identified only *mpk-1* (ref. 32). Furthermore, 53% of our identified genetic interactions would have been missed if the screens had been carried out in only one RNAi condition. In conclusion, using a sensitive method to screen a set of functionally related mutants with a relevant library allows building of a highly connected genetic network.

Our study represents the largest set of suppressor interactions yet identified in a metazoan. Suppressor interactions primarily connect genes with opposing functions, which are unlikely to have the same loss-of-function phenotypes. In contrast, phenotypic profiling screens connect genes on the basis of shared loss-of-function phenotypes[25,35]. This can explain why these two non-overlapping networks are complementary for recapitulating known functional interactions in cell polarity. A key output of our screening approach is the identification of relevant genes not easily found by phenotypic profiling. Secondary screens for enhancer/suppressor genetic profiles allowed us to select sets of candidates enriched for genes with polarity functions, observed either in sensitized backgrounds or by careful biophysical analyses. Phenotypic profiling may have missed these genes because their phenotype was masked by maternal sterility or their inhibition in a wild-type background was compensated by functional redundancy. Redundant mechanisms have been shown to operate in the initiation of cell polarity asymmetry in the early *C. elegans* embryo[15]. Through genetic interaction screening, we uncovered functional redundancy between two new cell polarity genes, *nop-1* and *plst-1*, demonstrating that genetic interaction screening can successfully identify functional redundant genes that are missed by single-gene knockdown analyses.

Focusing genetic suppressor screens across a biological process is a highly effective strategy for identifying a new landscape of functional relationships complementary to other large-scale functional data sets. The cell polarity genetic network that we generated using this approach will be an important resource for our understanding of cell polarity. As known cell polarity mechanisms are conserved in animals, many of the functional links identified here should be widely relevant. Finally, applying our screening strategy in other contexts will be a powerful way to identify key players and uncover new mechanisms in other essential biological processes. □

METHODS

Methods and any associated references are available in the online version of the paper.

Note: Supplementary Information is available in the online version of the paper

ACKNOWLEDGEMENTS

This work was supported by a Wellcome Trust Senior Research Fellowship (054523, to J.A.), postdoctoral fellowships from the Human Frontier Science Program (to B.T.F. and J.R.), a Herchel Smith Post-doctoral fellowship (to J.R.) and an EMBO fellowship (to B.T.F.). We thank P. Mains (Department of Biochemistry and Molecular Biology, University of Calgary, Canada) for providing *let-502(ts)* and *mel-11(ts)* mutants, and K. Kemphues (Department of Molecular Biology and Genetics, Cornell University, USA) for NMY-2-expressing bacteria. We thank F. Antigny, D. Lefer, V. Karabacak, S. Kroschwald, A. Maffioletti and A. Sayadian for their contribution in visual scoring and S. Fürthauer for help with hydrodynamic length measurements. We thank the media team of the Gurdon Institute for preparing screen reagents. We also thank C. Dix and R. Durbin for comments on the manuscript. Some nematode strains used in this work were provided by the Caenorhabditis Genetics Center, which is funded by the NIH National Center for Research Resources (NCRR). The P4A1 monoclonal antibody developed by J. Priess was obtained from the Developmental Studies Hybridoma Bank developed under the auspices of the NICHD and maintained by The University of Iowa, Department of Biology, Iowa City, IA 52242.

AUTHOR CONTRIBUTIONS

B.T.F. and J.R. designed and carried out the screen, analysed the network, characterized polarity candidates and drafted the manuscript. C.L. participated

in the primary screen experiments. S.N. and S.G. designed and performed the biophysical analysis of myosin regulators. E.Z. generated the GFP::NOP-1 transgenic strain. T.I. and M.S. isolated the *nmy-2(ts)* and *pkc-3(ts)* mutants. J.A. participated in the design and coordination of the study and edited the manuscript.

COMPETING FINANCIAL INTERESTS

The authors declare no competing financial interests.

Published online at www.nature.com/doifinder/10.1038/ncb2639
Reprints and permissions information is available online at www.nature.com/reprints

1. Lehner, B., Crombie, C., Tischler, J., Fortunato, A. & Fraser, A. G. Systematic mapping of genetic interactions in *Caenorhabditis elegans* identifies common modifiers of diverse signalling pathways. *Nat. Gen.* **38,** 896–903 (2006).
2. Byrne, A. B. *et al.* A global analysis of genetic interactions in *Caenorhabditis elegans*. *J. Biol.* **6,** 8 (2007).
3. Sandmann, T. & Boutros, M. Screens, maps networks: from genome sequences to personalized medicine. *Curr. Opin. Genet. Dev.* **22,** 36–44 (2012).
4. Costanzo, M. *et al.* The genetic landscape of a cell. *Science* **327,** 425–431 (2010).
5. Labbe, J. C., Pacquelet, A., Marty, T. & Gotta, M. A genomewide screen for suppressors of par-2 uncovers potential regulators of PAR protein-dependent cell polarity in *Caenorhabditis elegans*. *Genetics* **174,** 285–295 (2006).
6. O'Rourke, S. M., Dorfman, M. D., Carter, J. C. & Bowerman, B. Dynein modifiers in *C. elegans*: light chains suppress conditional heavy chain mutants. *PLoS Genet.* **3,** 1339–1354 (2007).
7. Dorfman, M., Gomes, J. E., O'Rourke, S. & Bowerman, B. Using RNA interference to identify specific modifiers of a temperature-sensitive, embryonic-lethal mutation in the *Caenorhabditis elegans* ubiquitin-like Nedd8 protein modification pathway E1-activating gene rfl-1. *Genetics* **182,** 1035–1049 (2009).
8. Coradini, D., Casarsa, C. & Oriana, S. Epithelial cell polarity and tumorigenesis: new perspectives for cancer detection and treatment. *Acta Pharmacol. Sin.* **32,** 552–564 (2011).
9. St Johnston, D. & Ahringer, J. Cell polarity in eggs and epithelia: parallels and diversity. *Cell* **141,** 757–774 (2010).
10. Gonczy, P. Mechanisms of asymmetric cell division: flies and worms pave the way. *Nat. Rev. Mol. Cell Biol.* **9,** 355–366 (2008).
11. Motegi, F. *et al.* Microtubules induce self-organization of polarized PAR domains in *Caenorhabditis elegans* zygotes. *Nat. Cell Biol.* **13,** 1361–1367 (2011).
12. Goldstein, B. & Hird, S. N. Specification of the anteroposterior axis in *Caenorhabditis elegans*. *Development* **122,** 1467–1474 (1996).
13. Cowan, C. R. & Hyman, A. A. Centrosomes direct cell polarity independently of microtubule assembly in *C. elegans* embryos. *Nature* **431,** 92–96 (2004).
14. Tsai, M. C. & Ahringer, J. Microtubules are involved in anterior–posterior axis formation in *C. elegans* embryos. *J. Cell Biol.* **179,** 397–402 (2007).
15. Zonies, S., Motegi, F., Hao, Y. & Seydoux, G. Symmetry breaking and polarization of the *C. elegans* zygote by the polarity protein PAR-2. *Development* **137,** 1669–1677 (2010).
16. Munro, E., Nance, J. & Priess, J. R. Cortical flows powered by asymmetrical contraction transport PAR proteins to establish and maintain anterior–posterior polarity in the early *C. elegans* embryo. *Dev. Cell* **7,** 413–424 (2004).
17. Motegi, F. & Sugimoto, A. Sequential functioning of the ECT-2 RhoGEF, RHO-1 and CDC-42 establishes cell polarity in *Caenorhabditis elegans* embryos. *Nat. Cell Biol.* **8,** 978–985 (2006).
18. Schonegg, S. & Hyman, A. A. CDC-42 and RHO-1 coordinate acto-myosin contractility and PAR protein localization during polarity establishment in *C. elegans* embryos. *Development* **133,** 3507–3516 (2006).
19. Boyd, L., Guo, S., Levitan, D., Stinchcomb, D. T. & Kemphues, K. J. PAR-2 is asymmetrically distributed and promotes association of P granules and PAR-1 with the cortex in *C. elegans* embryos. *Development* **122,** 3075–3084 (1996).
20. Watts, J. L. *et al.* par-6, a gene involved in the establishment of asymmetry in early *C. elegans* embryos, mediates the asymmetric localization of PAR-3. *Development* **122,** 3133–3140 (1996).
21. Goehring, N. W. *et al.* Polarization of PAR proteins by advective triggering of a pattern-forming system. *Science* **334,** 1137–1141 (2011).
22. Cuenca, A. A., Schetter, A., Aceto, D., Kemphues, K. & Seydoux, G. Polarization of the *C. elegans* zygote proceeds via distinct establishment and maintenance phases. *Development* **130,** 1255–1265 (2003).
23. Zipperlen, P., Fraser, A. G., Kamath, R. S., Martinez-Campos, M. & Ahringer, J. Roles for 147 embryonic lethal genes on C.elegans chromosome I identified by RNA interference and video microscopy. *EMBO J.* **20,** 3984–3992 (2001).
24. Piano, F. *et al.* Gene clustering based on RNAi phenotypes of ovary-enriched genes in *C. elegans*. *Curr. Biol.* **12,** 1959–1964 (2002).
25. Sonnichsen, B. *et al.* Full-genome RNAi profiling of early embryogenesis in *Caenorhabditis elegans*. *Nature* **434,** 462–469 (2005).
26. Piekny, A. J. & Mains, P. E. Rho-binding kinase (LET-502) and myosin phosphatase (MEL-11) regulate cytokinesis in the early *Caenorhabditis elegans* embryo. *J. Cell Sci.* **115,** 2271–2282 (2002).
27. Willis, J. H., Munro, E., Lyczak, R. & Bowerman, B. Conditional dominant mutations in the *Caenorhabditis elegans* gene act-2 identify cytoplasmic and muscle roles for a redundant actin isoform. *Mol. Biol. Cell* **17,** 1051–1064 (2006).
28. Rivers, D. M., Moreno, S., Abraham, M. & Ahringer, J. PAR proteins direct asymmetry of the cell cycle regulators Polo-like kinase and Cdc25. *J. Cell Biol.* **180,** 877–885 (2008).
29. Baas, A. F. *et al.* Activation of the tumour suppressor kinase LKB1 by the STE20-like pseudokinase STRAD. *EMBO J.* **22,** 3062–3072 (2003).
30. Kim, J. S., Hung, W., Narbonne, P., Roy, R. & Zhen, M. *C. elegans*STRADα and SAD cooperatively regulate neuronal polarity and synaptic organization. *Development* **137,** 93–102 (2010).
31. Tenlen, J. R., Molk, J. N., London, N., Page, B. D. & Priess, J. R. MEX-5 asymmetry in one-cell *C. elegans* embryos requires PAR-4- and PAR-1-dependent phosphorylation. *Development* **135,** 3665–3675 (2008).
32. Spilker, A. C., Rabilotta, A., Zbinden, C., Labbe, J. C. & Gotta, M. MAP kinase signalling antagonizes PAR-1 function during polarization of the early *Caenorhabditis elegans* embryo. *Genetics* **183,** 965–977 (2009).
33. Yoo, A. S., Bais, C. & Greenwald, I. Crosstalk between the EGFR and LIN-12/Notch pathways in *C. elegans* vulval development. *Science* **303,** 663–666 (2004).
34. Matsubara, Y. *et al.* The adaptor-like protein ROG-1 is required for activation of the Ras-MAP kinase pathway and meiotic cell cycle progression in *Caenorhabditis elegans*. *Gen. Cells* **12,** 407–420 (2007).
35. Green, R. A. *et al.* A high-resolution *C. elegans* essential gene network based on phenotypic profiling of a complex tissue. *Cell* **145,** 470–482 (2011).
36. Wright, A. J. & Hunter, C. P. Mutations in a β-tubulin disrupt spindle orientation and microtubule dynamics in the early *Caenorhabditis elegans* embryo. *Mol. Biol. Cell* **14,** 4512–4525 (2003).
37. Krueger, L. E., Wu, J. C., Tsou, M. F. & Rose, L. S. LET-99 inhibits lateral posterior pulling forces during asymmetric spindle elongation in *C. elegans* embryos. *J. Cell Biol.* **189,** 481–495 (2010).
38. Panbianco, C. *et al.* A casein kinase 1 and PAR proteins regulate asymmetry of a PIP(2) synthesis enzyme for asymmetric spindle positioning. *Dev. Cell* **15,** 198–208 (2008).
39. Collart, M. A. & Panasenko, O. O. The CCR4–NOT complex. *Gene* **492,** 42–53 (2012).
40. DeBella, L. R., Hayashi, A. & Rose, L. S. LET-711, the *Caenorhabditis elegans* NOT1 ortholog, is required for spindle positioning and regulation of microtubule length in embryos. *Mol. Biol. Cell* **17,** 4911–4924 (2006).
41. Schade, M. A., Reynolds, N. K., Dollins, C. M. & Miller, K. G. Mutations that rescue the paralysis of *Caenorhabditis elegans* ric-8 (synembryn) mutants activate the G α(s) pathway and define a third major branch of the synaptic signalling network. *Genetics* **169,** 631–649 (2005).
42. Liu, J., Maduzia, L. L., Shirayama, M. & Mello, C. C. NMY-2 maintains cellular asymmetry and cell boundaries, and promotes a SRC-dependent asymmetric cell division. *Dev. Biol.* **339,** 366–373 (2010).
43. Mayer, M., Depken, M., Bois, J. S., Julicher, F. & Grill, S. W. Anisotropies in cortical tension reveal the physical basis of polarizing cortical flows. *Nature* **467,** 617–621 (2010).
44. Rose, L. S., Lamb, M. L., Hird, S. N. & Kemphues, K. J. Pseudocleavage is dispensable for polarity and development in *C. elegans* embryos. *Dev. Biol.* **168,** 479–489 (1995).
45. Gally, C. *et al.* Myosin II regulation during *C. elegans* embryonic elongation: LET-502/ROCK, MRCK-1 and PAK-1, three kinases with different roles. *Development* **136,** 3109–3119 (2009).

METHODS

***C. elegans* strains.** Strains were grown at 15 °C unless otherwise stated. N2 (Bristol) was used as the wild type. All strains used in this study are listed in Supplementary Table S6.

Embryo and gonad development RNAi sub-library. According to Wormbase WS180, 2,721 genes are annotated as having an embryonic lethal phenotype (Emb) and 1,056 genes are annotated as having a sterile phenotype (Ste) when knocked down by RNAi in a wild-type or mutant background. Together, these identify 2,991 different genes. RNAi clones for 86% (2,573) of these genes from the Ahringer or ORFome libraries were available and constituted the screening library (2,632 clones; Supplementary Table S1)[46,47]. Of these clones, 2,209 have a single primary target as defined in Wormbase (at least 95% sequence identity with the RNAi clone over a minimum stretch of 100 nucleotides) and 423 have multiple primary targets, which knock down 172 additional unintended genes. In the WS220 version of Wormbase, 88% of the 2,573 Emb and Ste genes selected from WS180 are Emb or Ste in a wild-type background and 7% are Emb or Ste in a mutant background. The remaining 5% have changed annotation between WS180 and WS220 and are no longer referred to as Emb or Ste.

RNAi feeding conditions for suppressor screen of *ts* mutant in liquid. RNAi bacterial clones were inoculated from LB agar plates in 96-well format (10 μg ml^{-1} carbenicillin and 10 μg ml^{-1} tetracycline) to 900 μl LB liquid cultures (10 μg ml^{-1} carbenicillin, 10 μg ml^{-1} tetracycline and 100 U ml^{-1} nystatin) and grown overnight at 37 °C. Bacterial cultures were induced for 3 h with 4 mM final IPTG at 37 °C with agitation. To generate 10% or 40% dilutions of feeding bacteria (corresponding to weak and medium RNAi knockdown), liquid cultures were diluted with control bacteria (transformed with empty L4440 vector). Bacterial cultures were pelleted and re-suspended in half the culture volume in S-Basal solution (S-Basal medium with trace metals, 3 mM $MgSO_4$, 10 mM potassium citrate, 6 mM $CaCl_2$, 1 mM IPTG, 0.01% Triton X-100, 10 μg ml^{-1} carbenicillin, 10 μg ml^{-1} tetracycline, 100 U ml^{-1} nystatin and 0.1 μg ml^{-1} fungizone). Thirty microlitres of bacterial suspension was aliquoted into each well of a 96-well plate, then frozen and stored at −30 °C before use for feeding RNAi experiments.

Synchronized L1 larval populations were grown until the L4 larvae stage on OP50 bacteria on plates at 15°, and then L4 larvae were washed and resuspended in S-Basal solution. Thirty microlitres containing 10–15 worms was dispensed into each well of thawed RNAi bacterial feeding plates using a Wellmate liquid handler (Matrix). RNAi bacterial feeding plates with *ts* mutant worms were incubated for 72 h at the restrictive temperature. For each mutant, this was the temperature at which the hatching rate was about 1% (number of live progeny per well was between 5–15 L1s, background level) for at least 95% of wells of the 96-well plate (Supplementary Table S6). The number of progeny per well was estimated by visual inspection. Suppression was scored positive when the number of progeny in a well was more than 1.5 times the highest background level.

Suppressor reproducibility assessment. In a first step we tested each *ts* mutant for suppression by every RNAi library clone at three strengths (weak, medium and strong knockdown) in duplicate, generated from independent RNAi inductions ($n = 6$ tests). We selected RNAi clones if they showed suppression in at least 33% of the tests. We found an average of 146 candidate RNAi clones per mutant. In the second step, we retested all candidate clones at each RNAi strength three times in two independent experiments generated from independent RNAi induction ($n = 18$ tests). On the basis of these three independent experiments of 24 individual tests, RNAi clones were considered reproducible if they suppress embryonic lethality in 33% of all tests and in at least two independent experiments. This threshold allows the detection of RNAi clones that suppress only at one RNAi strength, which might differ slightly between independent RNAi inductions. We observed an average of 31 reproducible suppressors per mutant. In total, 356 different RNAi clones (13.5% of the original library) reproducibly suppressed at least one mutant (Supplementary Table S2).

Suppressor specificity assessment. The reproducible suppressor set will contain genes with polarity functions as well as genes where RNAi knockdown non-specifically suppresses a mutant. For example, it has been shown that *ts* mutants can be nonspecifically suppressed by RNAi knockdowns of genes enriched for mitochondrial and ribosomal functions[6]. To identify nonspecific suppressors, we carried out a third step for specificity by testing the reproducible suppressors for their ability to suppress any of five different *ts* mutants not involved in polarity. In this step, all reproducible clones were tested in two independent experiments consisting of three RNAi conditions in triplicate (18 tests). A reproducible clone was classified as nonspecific if it showed a suppression phenotype for at least 22% of the 18 tests with any non-polarity *ts* mutant (Supplementary Table S2). Out of these analyses we classified the 356 reproducible clones into two sets, 300 specific and 56 nonspecific (Supplementary Table S2).

Mapping RNAi clones to genes. The 356 reproducible clones were sequenced and their primary target gene(s) mapped using *C. elegans* reference genome WS210 (Supplementary Tables S1 and S2). Primary RNAi target genes have at least 95% sequence identity with the RNAi clone over a minimum stretch of 100 nucleotides. Genes knocked down by an RNAi clone with multiple targets are labelled as multiple targets in Supplementary Table S3. These genes were omitted from the functional class statistical analysis (Supplementary Table S4) and the graphical network representations (Figs 2 and 3).

Functional class analysis. Specific and nonspecific suppressors were manually assigned a functional class and a sub-functional category using information derived from Wormbase (WS210), BlastP matches, Treefam phylogenies, protein domain homology, Gene Ontology terms and KOGs (Eukaryotic Clusters of Orthologous Groups; Supplementary Table S4). Functional enrichments were statistically analysed using Fisher's exact test. In agreement with the results of ref. 6, the functional analysis of our suppressors showed enrichment for mitochondrial and ribosomal functions. Therefore, we removed suppressors functionally labelled as cytoplasmic or mitochondrial ribosomal genes and respiratory chain genes from our network representation and further analysis.

Network representation. Graphical network representations were plotted using Cytoscape[48]. Our data are compared with embryo and gonad phenotypic interactions[35] with a connection specificity index greater than or equal to 0.96.

Quantitative enhancer screen on agar plate. RNAi feeding bacteria were grown and induced as described for liquid suppressor screens. Fifty microlitres of induced bacteria was spotted onto each well of a 6-well LB (10 μg ml^{-1} carbenicillin, 10 μg ml^{-1} tetracycline and 100 U ml^{-1} nystatin) agar plate containing 1 mM IPTG. Three L4 larvae were added per well. Wild-type worms and *ts* mutants of interest were incubated in parallel for 48–72 h at a semi-permissive temperature. Each RNAi reagent was tested at least in two independent experiments in duplicate. The hatching ratio was calculated by dividing the number of live progeny by the number of eggs laid. This ratio was used as a proxy for fitness (W) in the enhancement tests. At the semi-permissive temperatures used, mutant fitness (W_{mut}) grown on control bacteria was greater than 0.25 with more than 50 live progeny per well. We called W_{obs} the fitness observed after RNAi in the *ts* mutant and W_{RNAi} the fitness observed in the same RNAi condition in the wild type. We calculated the expected fitness (W_{exp}) for non-interacting genes by the product of W_{mut} multiplied by W_{RNAi}($W_{exp} = W_{mut} \times W_{RNAi}$). We represent the strength of a genetic interaction by epsilon (ε), the deviation of the observed fitness from the expected one ($\varepsilon = W_{obs} - W_{exp}$). A negative value for ε indicates an enhancement. We focus our analysis on strong enhancers where $\varepsilon \leq -0.15$ and Z-test $P < 0.001$.

Immunofluorescence microscopy. Immunofluorescence microscopy was performed as previously described[28]. All antibodies used in this study are listed in Supplementary Table S7. DNA was DAPI stained. Images were acquired using a Carl Zeiss LSM510 Meta confocal microscope equipped with LSM image software and a Carl Zeiss Axioplan2 microscope with Open Lab image software.

Polarity phenotype quantification and analysis. The average of the AB cell percentage area was calculated by determining the area of the AB cell with respect to the total embryo area (AB + P1) in at least 15 two-cell stage embryos. Statistical analyses were done using Student's *t*-test.

The percentage of PAR-2 aberrant localization in two-cell stage embryos was determined by assessing PAR-2 localization blind to RNAi treatment. These data were statistically analysed using Fisher's exact test.

The MEX-5 intensity ratio was determined by measuring the mean greyscale value for a fixed area (625 pixels^2) in AB and P1 cells. We counted how many embryos for each RNAi condition showed a MEX-5 intensity ratio (AB/P1) inferior to the minimum value observed in the control. These data were statistically analysed using Fisher's exact test.

To determine *nop-1(it142)* and *plst-1* enhancement of symmetric first cell divisions we counted how many embryos for each RNAi condition showed an AB cell percentage area inferior to the minimum value observed in the control. These data were statistically analysed using Fisher's exact test.

NMY-2::GFP movie acquisition. Confocal movies of cortical NMY-2::GFP were acquired at 22–24 °C with a spinning-disc confocal microscope using a Zeiss C-Apochromat 63×/1.2 NA objective lens, a Yokogawa CSU-X1 scan head and an Andor iXon electron-multiplying CCD (charge-coupled device) camera (512 by 512 pixels). A stack consisting of three *z*-planes (0.5 μm spacing) with an exposure of 150 ms using a 488 nm laser was acquired at an interval of 5 s from the onset of cortical flow until the first cell division. The maximum intensity projection of the stack at each time point was then subjected to further analysis. In addition, a single

DOI: 10.1038/ncb2639

bright-field image was acquired in the mid plane of the embryo at an interval of 15 s. Image analysis was performed with ImageJ and MATLAB.

Quantification of flow velocity and density profiles. Cortical flow velocities of NMY-2::GFP in the acquired movies were quantified using particle image velocimetry as described in ref. 49. Briefly, each frame was divided into templates using a square grid (6 μm by 6 μm). A two-dimensional flow field was generated by identifying the best match for each template square in the following frame, using the normxcorr2 cross-correlation function from MATLAB, and by defining the vector to be the displacement of the template square. To project the two-dimensional flow field on the anterior–posterior axis, the embryo was divided into 12 bins along the anterior–posterior axis, and the average magnitude of individual velocity vectors over 20 consecutive frames was calculated. To avoid boundary effects, the posterior- and anterior-most bins were excluded, and averages were computed along a 12-μm-thick stripe in the centre of the embryo. The averages of the magnitude of velocity in each bin were then averaged over all embryos of one experimental condition to generate the heat maps. The averages of the magnitude of all velocity vectors within the 12-μm-thick stripe, covering the 10 central bins, were calculated to provide the average magnitude velocity. We obtained the anterior–posterior myosin density profiles in the same bins by averaging the normalized fluorescence intensities in each bin across the 12-μm-thick stripe, for the purpose of obtaining the range of flow (see below).

Estimation of the range of flow. To estimate the range of flow using a hydrodynamic description of the cortex[43], we chose the time of 30% cortical retraction of NMY-2::GFP, and the anterior–posterior velocity and myosin density profiles were quantified in this period over 20 consecutive frames for each embryo. Using a hydrodynamic description of the actomyosin cell cortex in the framework of active fluids[43], we determined the theoretical flow profile that most closely matched the experimentally quantified anterior–posterior velocity given the measured myosin density profile[43] for each individual embryo, through variation of both the hydrodynamic length (that is, the range of flow) and the coefficient that converts myosin intensity to active tension (we assume a linear relationship). For each experimental condition, we report the ensemble average of the ranges of flow obtained for each individual embryo, and the respective standard error.

Quantification of the myosin intensity coefficient of variation. The coefficient of variation (c_v) of NMY-2::GFP fluorescence intensities is a measure of dispersion of fluorescence in the embryo and is the ratio of the standard deviation of fluorescence intensities and the mean fluorescence intensities. A homogeneous distribution of fluorescence intensity within the embryo will result in a small c_v and a higher c_v will result from a patchy cortex with very bright foci-like structures interspersed with less bright regions. For obtaining the c_v of fluorescence intensities in each embryo, the boundary of the embryo was determined and the mean and s.d. of fluorescence intensities in the entire embryo in 10 frames at the onset of cortical flows was utilized. We report the ensemble average and standard error for each experimental condition.

46. Kamath, R. S. *et al*. Systematic functional analysis of the *Caenorhabditis elegans* genome using RNAi. *Nature* **421,** 231–237 (2003).
47. Rual, J. F. *et al*. Toward improving *Caenorhabditis elegans* phenome mapping with an ORFeome-based RNAi library. *Gen. Res.* **14,** 2162–2168 (2004).
48. Shannon, P. *et al*. Cytoscape: a software environment for integrated models of biomolecular interaction networks. *Gen. Res.* **13,** 2498–2504 (2003).
49. Raffel, M. *Particle Image Velocimetry: a Practical Guide* 2nd edn (Springer, 2007).

DOI: 10.1038/ncb2639

nature cell biology

a

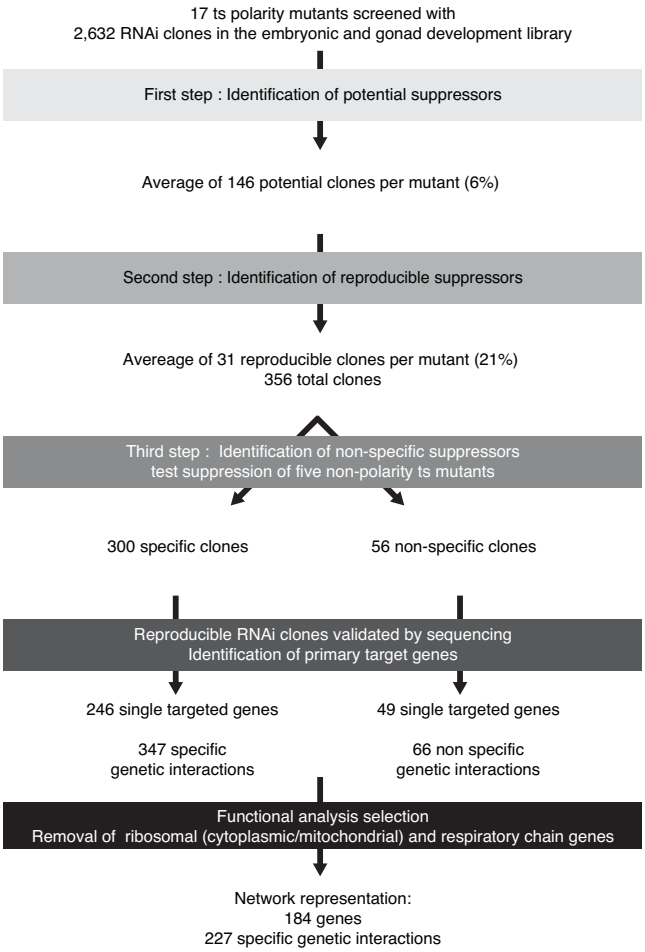

b

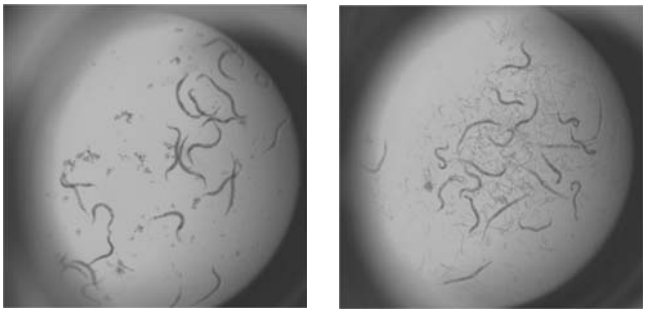

Figure S1 Screening steps and example of positive and negative hits, related to Figure 1. (a) Flowchart containing the screening steps followed (b) Pictures of *pkc-3(ts)* mutant at the non-permissive temperature after 72h of RNAi by feeding with empty vector control (left) and *par-2* RNAi clone (right).

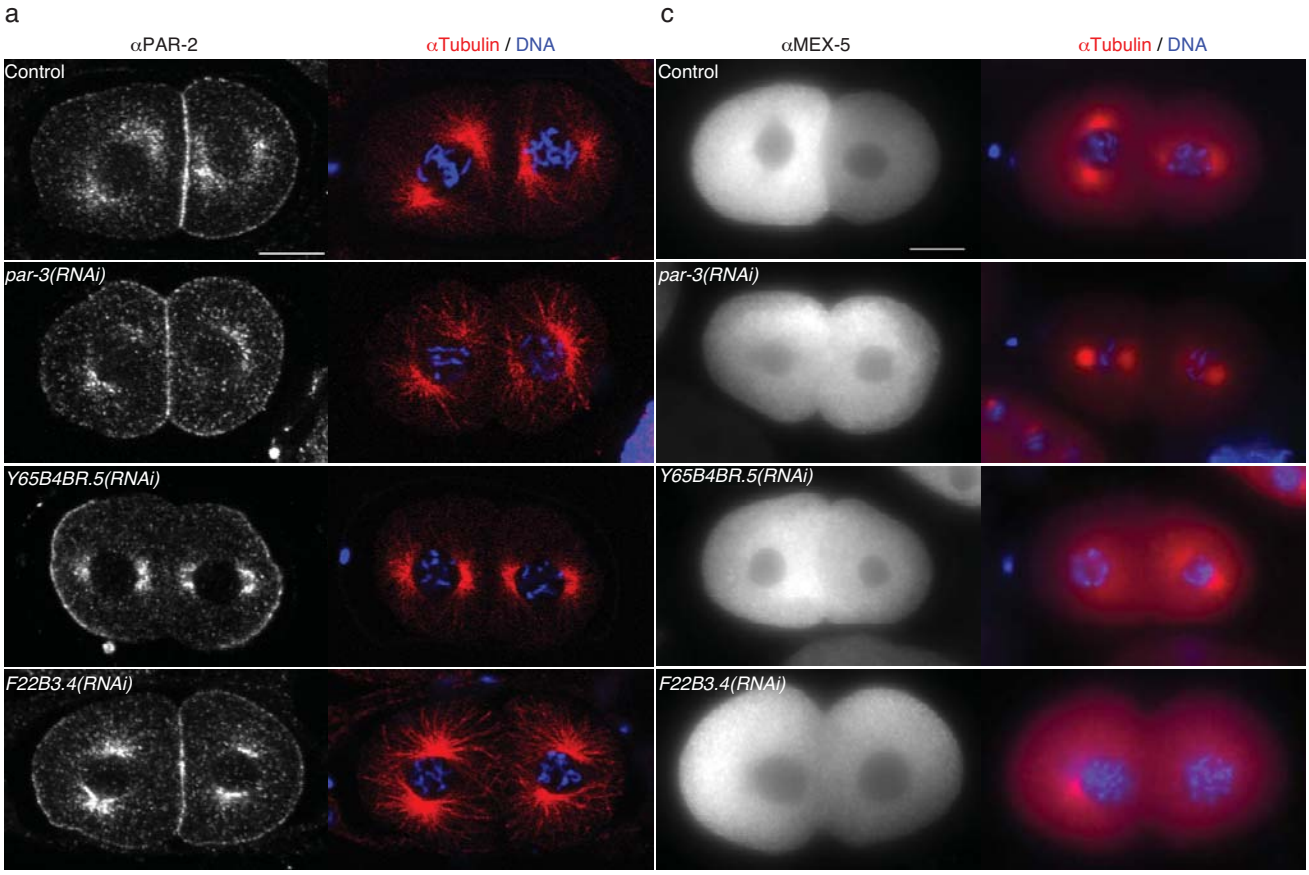

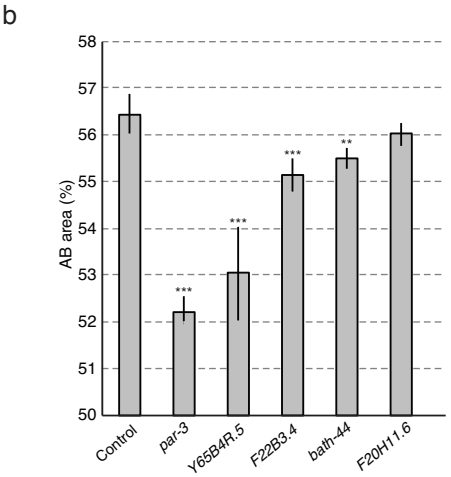

d

	Embryos with PAR-2 mislocalised			Embryos with MEX-5 ratio < 1.2		
Control	52%		n=29	0%		n=106
par-3	100%	**	n=8	70%	***	n=90
Y65B4BR.5	85%	*	n=20	12%	**	n=91
F22B3.4	81%	*	n=37	15%	**	n=96
bath-44	68%	ns	n=25	8%	ns	n=25
F20H11.6	65%	ns	n=20	1%	ns	n=143

Figure S2 Cell size asymmetry quantification and phenotypes of PAR regulators, related to Figure 5. (a) Midsection of two-cell stage *pkc-3(ts)* embryos stained for PAR-2 (left panel) and tubulin (red) / DNA (DAPI, blue) (right panel). Posterior cortical localisation of PAR-2 (as observed in *pkc-3(ts)* control) is lost in *par-3*, Y65B4R.5 and F22B3.4 RNAi. Scale bar: 10μm. (b) Bar graph with the average percentage of embryo area occupied by the anterior cell AB (± sem) for each RNAi conditions in *pkc-3(ts)*. We observed a significant loss of cell asymmetry for *par-3*, Y65B4R.5, F22B3.4 and *bath-44* RNAi. **p<0.01, ***p<0.001 by Student's *t* test. (c) Fluorescent images of two-cell stage *pkc-3(ts)* embryos stained for the cell fate determinant MEX-5 (left panel) and tubulin (red) / DNA (DAPI, blue) (right panel). MEX-5 anterior cytoplasm localisation (as observed in *pkc-3(ts)* control) is disrupted in *par-3*, Y65B4R.5 and F22B3.4 RNAi. Scale bar: 10μm. (d) Table indicating the percentage of embryos with PAR-2 mislocalised or MEX-5 intensity ratio (anterior cell AB versus posterior cell P1) inferior to 1.2. PAR-2 is significantly mislocalised in *par-3*, Y65B4R.5 and F22B3.4 RNAi and MEX-5 ratio is significantly perturbed in *par-3*, Y65B4R.5 and F22B3.4 RNAi. *p<0.05, **p<0.01, ***p<0.001 by Fisher's exact test.

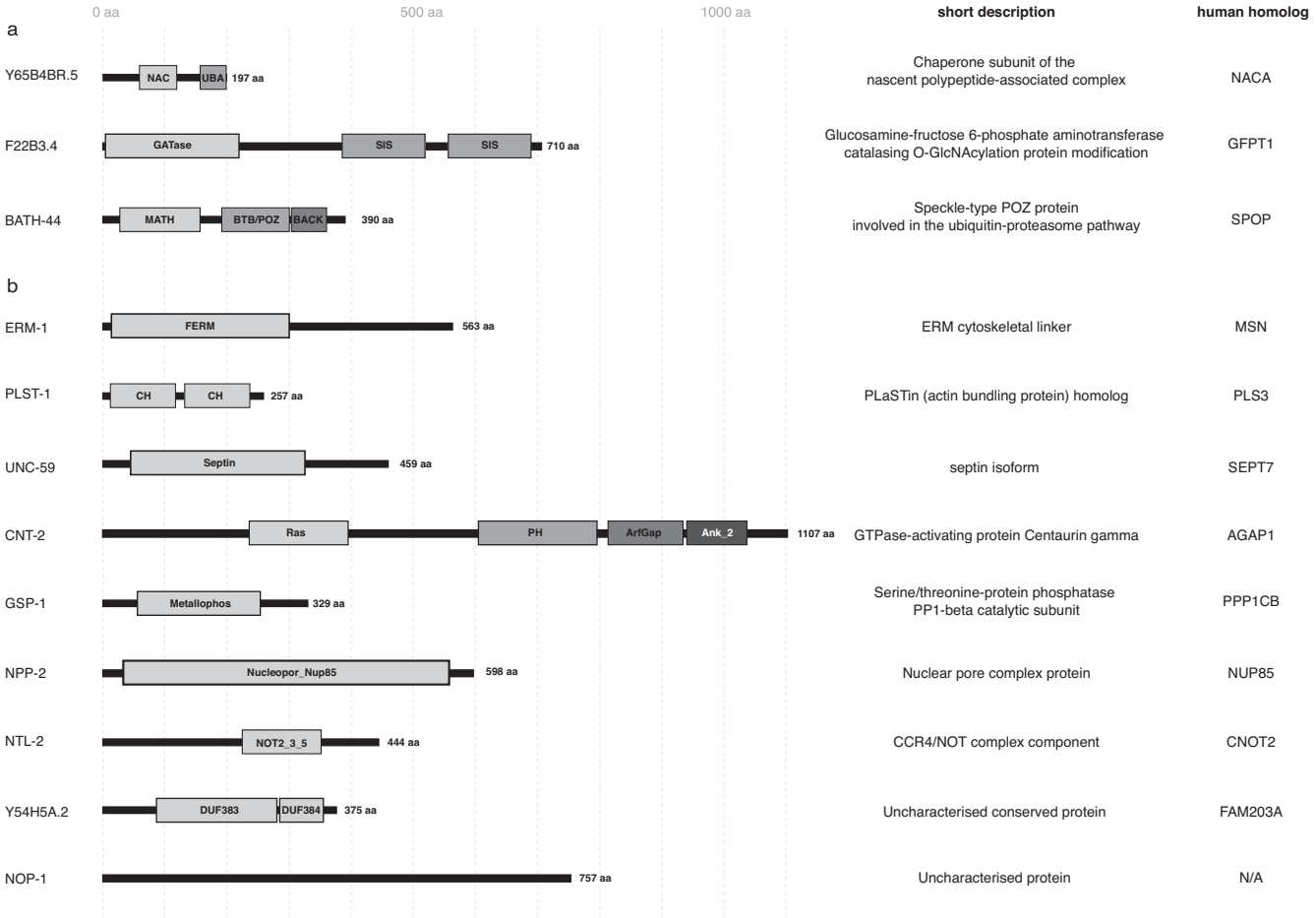

Figure S3 Schematic representation of the novel regulators characterised in this study indicating their conserved functional domains and their potential cellular functions. (a) PAR proteins regulators with their identified domains: NAC (nascent polypeptide-associated complex), UBA (uniquitin associated domain), GATase (glutamine amidotransferases), SIS (sugar isomerase), MATH (meprin and TRAF homology domain), BTB (broad-complex, tramtrack and bric a brac) POZ (Pox virus and Zinc finger), BACK (BTB And C-terminal Kelch). (b) Myosin regulators with their identified domains: FERM (4.1 protein, ezrin, radixin and moesin), CH (calponin homology domain), Septin (Septin homology domain), Ras (Ras homology domain), PH (Pleckstrin homology domain), ArfGAP (Putative GTPase activating protein for Arf), Ank_2 (ankyrin repeat), Metallophos (Calcineurin-like phosphoesterase), Nucleopor_Nup85 (Nup85 Nucleoporin), NOT2_3_5 (NOT2 / NOT3 / NOT5 family), DUF (domain of unknown function).

a

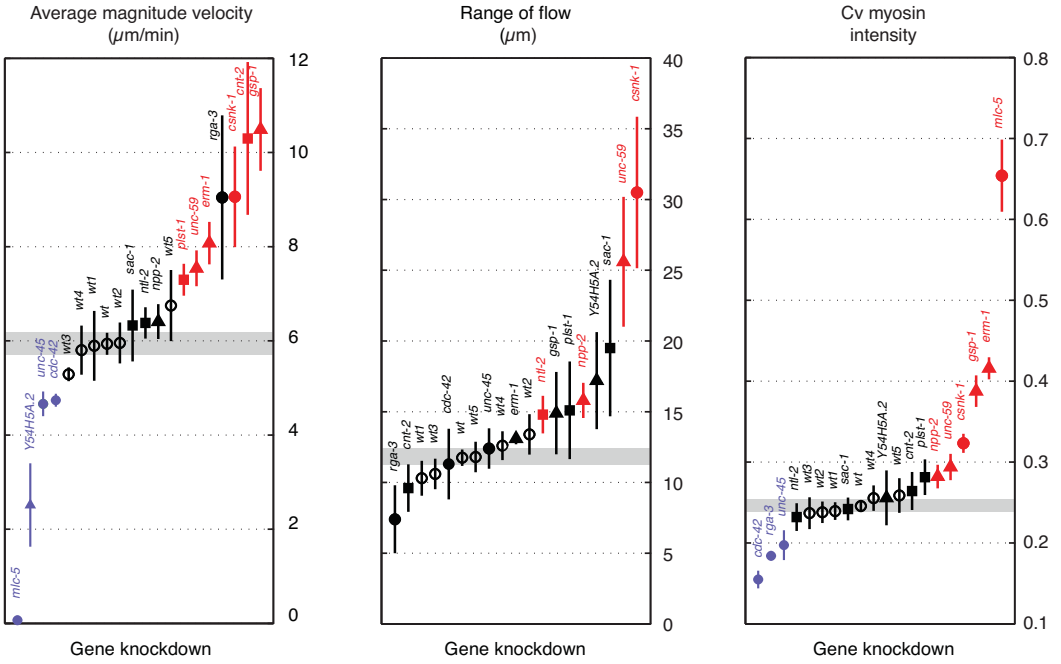

b

Gene knock-down	Actomyosin regulator category	Average magnitude velocity (μm/min)	Range of flow (μm)	CV myosin intensity	Short description
wt	Control	5.9 ± 0.2	11.8 ± 0.6	0.25 ± 0.01	See Fig. S5a-d and movie S1
wt1		5.9 ± 0.7	10.3 ± 1.2	0.24 ± 0.01	
wt2		6 ± 0.4	13.4 ± 1.4	0.24 ± 0.01	
wt3		5.3 ± 0.1	10.6 ± 1.1	0.24 ± 0.02	
wt4		5.8 ± 0.5	12.6 ± 1	0.26 ± 0.02	
wt5		6.7 ± 0.8	11.8 ± 1.1	0.26 ± 0.02	
cdc-42	Known actomyosin regulator	4.7 ± 0.1	11.3 ± 2.5	0.15 ± 0.01	Smaller foci with reduced velocity, see Fig. S5e and movie S2
csnk-1		9.1 ± 1.1	30.5 ± 5.4	0.32 ± 0.01	Increased focal density and orthogonal velocity, see Fig. S5f and movie S3
mlc-5		0.1 ± 0.03	NA	0.65 ± 0.04	No foci, immobile puncta, see Fig. S5g and movie S4
rga-3		9 ± 1.7	7.4 ± 2.4	0.18 ± 0.01	No foci, NMY-2 more homogenous at the cortex, see Fig. S5h
unc-45		4.7 ± 0.3	12.4 ± 1.4	0.2 ± 0.02	Slight reduction in focal density and focal velocity, see Fig. S5i and movie S5
cnt-2	act-2(ts) suppressor nmy-2(ts) enhancer	10.3 ± 1.6	9.6 ± 1.7	0.26 ± 0.02	Increased focal velocity, see Fig. S5j and movie S10
ntl-2		6.4 ± 0.3	14.8 ± 1.3	0.23 ± 0.02	Range of flow altered
plst-1		7.3 ± 0.3	15.1 ± 3.5	0.28 ± 0.02	Decreased focal size and increased focal velocity, see Fig. S5l movie S7
sac-1		6.3 ± 0.8	19.5 ± 4.8	0.24 ± 0.01	No detectable defect, see Fig. S5m
erm-1	nmy-2(ts) suppressor act-2(ts) enhancer	8.1 ± 0.5	13.1 ± 0.4	0.42 ± 0.01	Increased focal velocity, see Fig. S5n and movie S9
gsp-1		10.5 ± 0.9	14.9 ± 2.9	0.39 ± 0.02	Increased focal velocity, see Fig. S5o and movie S11
npp-2		6.4 ± 0.4	15.8 ± 1.2	0.28 ± 0.01	Slight reduction in focal density, see Fig. S5p
unc-59		7.5 ± 0.4	25.6 ± 4.6	0.29 ± 0.02	Slight reduction in focal density, larger foci with increased velocity, see Fig. S5q and movie S8
Y54H5A.2		2.5 ± 0.9	17.2 ± 3.4	0.26 ± 0.03	Decreased focal velocity, see Fig. S5r and movie S6

Figure S4 Biophysical characterisation including analysis of five groups of wt controls, related to Figure 6. (a) Five independent groups of wild type movies (wt1 to wt5) were randomly generated from 25 wt acquisitions. All 14 RNAi conditions and the 5 different wt control groups were tested for significant difference to the wt group containing all 25 wild type movies (95% confidence). None of the five wild type groups display measures that are significantly different from the combined wt data set. (b) Table includes average magnitude velocity, range of flow and CV myosin intensity values after RNAi of actomyosin regulators. Errors indicate standard error of the mean. *mlc-5*(RNAi) shows no cortical flow, therefore no range of flow could be calculated. Significant defects are reported in blue (decreased) and in red (increased). A short description of the NMY-2::GFP phenotypes observed after RNAi is also indicated.

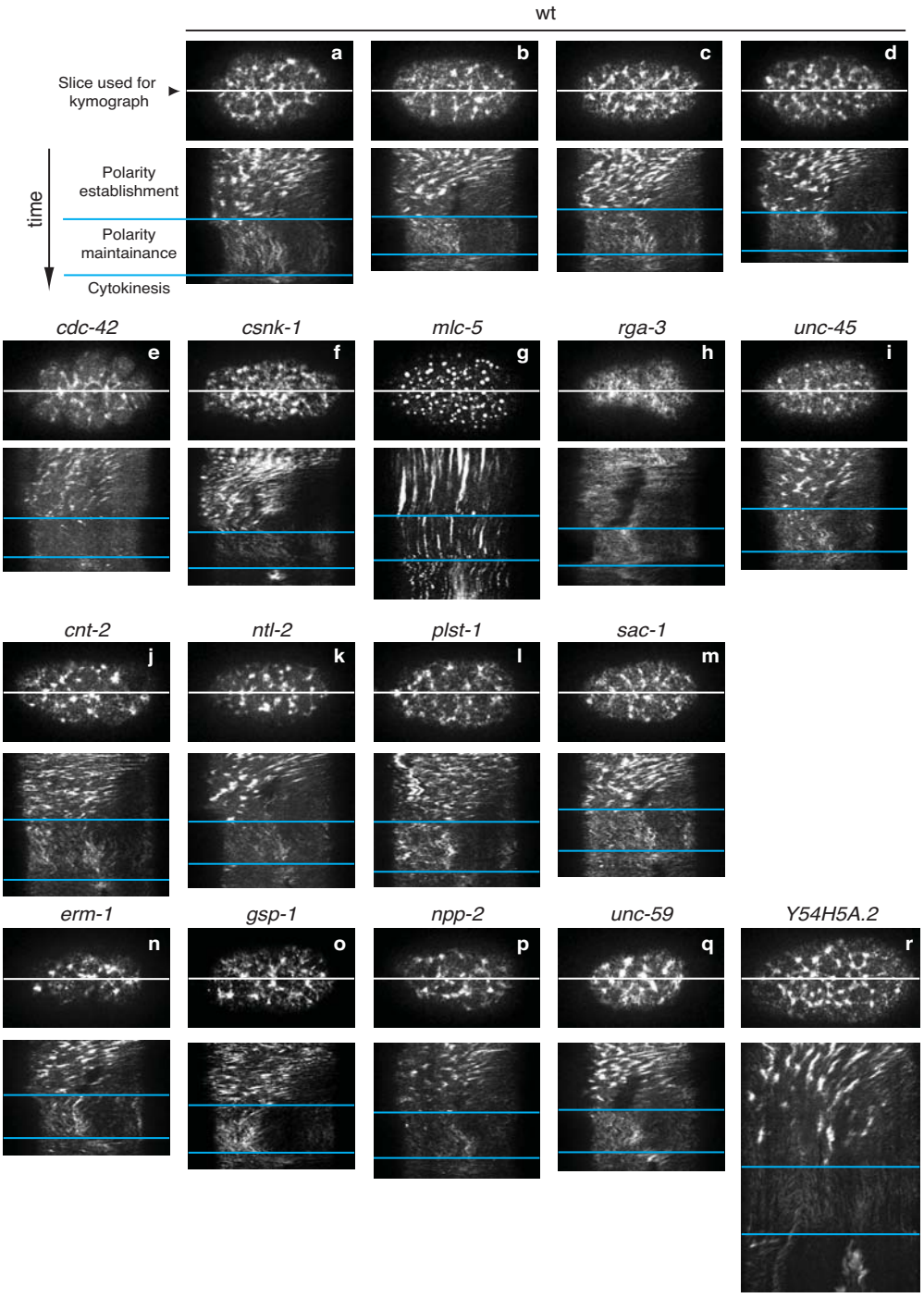

Figure S5 Kymographs of NMY-2 cortical retraction for novel actomyosin regulators, related to Figure 6. For each RNAi and four wild type movies (wt) we show a representative picture at the onset of polarity and a kymograph of a middle slice of the embryo from polarity establishment until cytokinesis (a-r).

Supplementary Videos

Video S1 Time-lapse movie of NMY-2::GFP expressed in a wild-type control embryo
Cortical projection of NMY-2::GFP in a wild-type control embryo. Images were acquired every 5s.

Video S2 Time-lapse movie of NMY-2::GFP expressed in a *cdc-42(RNAi)* embryo
Cortical projection of NMY-2::GFP in a *cdc-42(RNAi)* embryo. Images were acquired every 5s.

Video S3 Time-lapse movie of NMY-2::GFP expressed in a *csnk-1(RNAi)* embryo
Cortical projection of NMY-2::GFP in a *csnk-1(RNAi)* embryo. Images were acquired every 5s.

Video S4 Time-lapse movie of NMY-2::GFP expressed in a *mlc-5(RNAi)* embryo
Cortical projection of NMY-2::GFP in a *mlc-5(RNAi)* embryo. Images were acquired every 5s.

Video S5 Time-lapse movie of NMY-2::GFP expressed in a *unc-45(RNAi)* embryo
Cortical projection of NMY-2::GFP in a *unc-45(RNAi)* embryo. Images were acquired every 5s.

Video S6 Time-lapse movie of NMY-2::GFP expressed in a *Y54H5A.2(RNAi)* embryo
Cortical projection of NMY-2::GFP in a *Y54H5A.2(RNAi)* embryo. Images were acquired every 5s.

Video S7 Time-lapse movie of NMY-2::GFP expressed in a *plst-1(RNAi)* embryo
Cortical projection of NMY-2::GFP in a *plst-1(RNAi)* embryo. Images were acquired every 5s.

Video S8 Time-lapse movie of NMY-2::GFP expressed in a *unc-59(RNAi)* embryo
Cortical projection of NMY-2::GFP in a *unc-59(RNAi)* embryo. Images were acquired every 5s.

Video S9 Time-lapse movie of NMY-2::GFP expressed in a *erm-1(RNAi)* embryo
Cortical projection of NMY-2::GFP in a *erm-1(RNAi)* embryo. Images were acquired every 5s.

Video S10 Time-lapse movie of NMY-2::GFP expressed in a *cnt-2(RNAi)* embryo
Cortical projection of NMY-2::GFP in a *cnt-2(RNAi)* embryo. Images were acquired every 5s.

Video S11 Time-lapse movie of NMY-2::GFP expressed in a *gsp-1(RNAi)* embryo
Cortical projection of NMY-2::GFP in a *gsp-1(RNAi)* embryo. Images were acquired every 5s.

Video S12 Time-lapse movie of NMY-2::GFP expressed in a *nop-1(RNAi)* embryo
Cortical projection of NMY-2::GFP in a *nop-1(RNAi)* embryo. Images were acquired every 5s.

Supplementary Tables

Table S1 List of RNAi clones present in the embryonic and gonad development RNAi library, related to Figure 1.
Table includes: RNAi clone name, pcr product name (name used in Wormbase), number and list of targeted genes. Primary targets have sequence identity to the RNAi probe of at least 95% over a stretch of at least 100 nucleotides (as defined in wormbase).

Table S2 Screening results obtained for reproducibility and specificity steps, related to Figure 1.
Worksheets include the list of RNAi clones tested in the reproducibility and specificity steps. In the 'reproducibility_step' sheet, we report for each clone the polarity ts mutant suppressed and the percentage of tests showing suppression phenotype in each experiment. Summary table contains the number of suppressing clones obtained for each mutant. In the 'specificity_step' sheet, we report for each clone the percentage of tests showing suppression phenotype for non-polarity mutant. The summary tables contain the results for the non-polarity ts mutants (red) and the number of clones specifically suppressing the polarity mutants of interest (green). 'interactions_summary' sheet contains all the reproducible interactions reporting the RNAi clone used and the polarity mutant screened. 'clones_summary' sheet contains all the 356 reproducible clones found in this study indicating which ones were considered specific. Reproducible clones were verified by sequencing and primary targeted genes were mapped against *C. elegans* genome (WS210).

Table S3 Sets of suppressors and interactions found for the 14 polarity seeds, related to Figure 1-3. Worksheets include suppressor properties (gene names, RNAi clones with unique/multiple targets, specificity step result, functional & subfunctional categories and ts mutants suppressed) for different suppressors sets analysed in our study: 427 total suppressors, 246 suppressors uniquely targeted and specific, 49 suppressors uniquely targeted and non-specific, 67 suppressors classified as ribosome & respiratory chain and 179 suppressors plotted in our network. For the final 179 genes set, the table reports known human homologue (retrieved using ensembl compara and KEGG dataset), previous polarity involvement and RNAi phenotype found in large-scale phenotypic screens[1-8]. For a more detail classification of RNAi phenotypes see 'RNAi_phenotype_classification' sheet. '227_interactions_in_network' worksheet contains the final list of suppression interactions represented in Figure 2 and Figure 3C.

Table S4 Suppressor functional class analysis, related to Figure 2. All genes were manually assigned a functional class and a sub-functional category using information derived from Wormbase WS210 including BlastP matches, Treefam phylogenies, protein domain homology, GO term and KOGs information. 'Functionalclass_enrich_Nspe_set' sheet contains the suppressor distribution between the different functional classes and sub functional categories found in our network. Only suppressor targeted by RNAi clone with unique target are analysed. By comparing the suppressors from the 295 reproducible set and the 49 non-specific set, we observed a clear enrichment for ribosomal protein cytoplasmic gene in the non-specific set. (p-value by Fisher's exact test) 'Functionalclass_enrich_spe_set' sheet contains for each ts mutant the distribution of specific reproducible suppressors into each functional class and sub-category. Enrichment of genes in any category for each polarity ts mutant is indicated in red (p-value by Fisher's exact test)

Table S5 Known polarity genes and their reported functional links related to Figure 3.

Table S6 List of strains used in this study.

Table S7 List of antibodies used in this study.

Supplementary references (cited in Supplementary Tables)

1. Fraser, A.G. *et al.* Functional genomic analysis of C. elegans chromosome I by systematic RNA interference. *Nature* **408**, 325-330 (2000).
2. Zipperlen, P., Fraser, A.G., Kamath, R.S., Martinez-Campos, M. & Ahringer, J. Roles for 147 embryonic lethal genes on C.elegans chromosome I identified by RNA interference and video microscopy. *EMBO J* **20**, 3984-3992 (2001).
3. Kamath, R.S. *et al.* Systematic functional analysis of the Caenorhabditis elegans genome using RNAi. *Nature* **421**, 231-237 (2003).
4. Rual, J.F. *et al.* Toward improving Caenorhabditis elegans phenome mapping with an ORFeome-based RNAi library. *Genome Res* **14**, 2162-2168 (2004).
5. Sonnichsen, B. *et al.* Full-genome RNAi profiling of early embryogenesis in Caenorhabditis elegans. *Nature* **434**, 462-469 (2005).
6. Piano, F. *et al.* Gene clustering based on RNAi phenotypes of ovary-enriched genes in C. elegans. *Curr Biol* **12**, 1959-1964 (2002).
7. Gonczy, P. *et al.* Functional genomic analysis of cell division in C. elegans using RNAi of genes on chromosome III. *Nature* **408**, 331-336 (2000).
8. Maeda, I., Kohara, Y., Yamamoto, M. & Sugimoto, A. Large-scale analysis of gene function in Caenorhabditis elegans by high-throughput RNAi. *Curr Biol* **11**, 171-176 (2001).
9. Tabuse, Y. *et al.* Atypical protein kinase C cooperates with PAR-3 to establish embryonic polarity in Caenorhabditis elegans. *Development* **125**, 3607-3614 (1998).
10. Watts, J.L. *et al.* par-6, a gene involved in the establishment of asymmetry in early C. elegans embryos, mediates the asymmetric localization of PAR-3. *Development* **122**, 3133-3140 (1996).
11. Munro, E., Nance, J. & Priess, J.R. Cortical flows powered by asymmetrical contraction transport PAR proteins to establish and maintain anterior-posterior polarity in the early C. elegans embryo. *Dev Cell* **7**, 413-424 (2004).
12. Etemad-Moghadam, B., Guo, S. & Kemphues, K.J. Asymmetrically distributed PAR-3 protein contributes to cell polarity and spindle alignment in early C. elegans embryos. *Cell* **83**, 743-752 (1995).
13. Wu, J.C. & Rose, L.S. PAR-3 and PAR-1 inhibit LET-99 localization to generate a cortical band important for spindle positioning in Caenorhabditis elegans embryos. *Mol Biol Cell* **18**, 4470-4482 (2007).
14. Bellanger, J.M. & Gonczy, P. TAC-1 and ZYG-9 form a complex that promotes microtubule assembly in C. elegans embryos. *Curr Biol* **13**, 1488-1498 (2003).
15. Le Bot, N., Tsai, M.C., Andrews, R.K. & Ahringer, J. TAC-1, a regulator of microtubule length in the C. elegans embryo. *Curr Biol* **13**, 1499-1505 (2003).
16. Srayko, M., Quintin, S., Schwager, A. & Hyman, A.A. Caenorhabditis elegans TAC-1 and ZYG-9 form a complex that is essential for long astral and spindle microtubules. *Curr Biol* **13**, 1506-1511 (2003).
17. Piekny, A.J. & Mains, P.E. Rho-binding kinase (LET-502) and myosin phosphatase (MEL-11) regulate cytokinesis in the early Caenorhabditis elegans embryo. *J Cell Sci* **115**, 2271-2282 (2002).
18. Tenlen, J.R., Molk, J.N., London, N., Page, B.D. & Priess, J.R. MEX-5 asymmetry in one-cell C. elegans embryos requires PAR-4- and PAR-1-dependent phosphorylation. *Development* **135**, 3665-3675 (2008).
19. Afshar, K. *et al.* RIC-8 is required for GPR-1/2-dependent Galpha function during asymmetric division of C. elegans embryos. *Cell* **119**, 219-230 (2004).
20. Schubert, C.M., Lin, R., de Vries, C.J., Plasterk, R.H. & Priess, J.R. MEX-5 and MEX-6 function to establish soma/germline asymmetry in early C. elegans embryos. *Mol Cell* **5**, 671-682 (2000).
21. Jenkins, N., Saam, J.R. & Mango, S.E. CYK-4/GAP provides a localized cue to initiate anteroposterior polarity upon fertilization. *Science* **313**, 1298-1301 (2006).
22. Motegi, F. & Sugimoto, A. Sequential functioning of the ECT-2 RhoGEF, RHO-1 and CDC-42 establishes cell polarity in Caenorhabditis elegans embryos. *Nat Cell Biol* **8**, 978-985 (2006).
23. Motegi, F. *et al.* Microtubules induce self-organization of polarized PAR domains in Caenorhabditis elegans zygotes. *Nat Cell Biol* **13**, 1361-1367 (2011).
24. Tsou, M.F., Hayashi, A. & Rose, L.S. LET-99 opposes Galpha/GPR signaling to generate asymmetry for spindle positioning in response to PAR and MES-1/SRC-1 signaling. *Development* **130**, 5717-5730 (2003).
25. Rivers, D.M., Moreno, S., Abraham, M. & Ahringer, J. PAR proteins direct asymmetry of the cell cycle regulators Polo-like kinase and Cdc25. *J Cell Biol* **180**, 877-885 (2008).
26. Nishi, Y., Rogers, E., Robertson, S.M. & Lin, R. Polo kinases regulate C. elegans embryonic polarity via binding to DYRK2-primed MEX-5 and MEX-6. *Development* **135**, 687-697 (2008).
27. Beatty, A., Morton, D. & Kemphues, K. The C. elegans homolog of Drosophila Lethal giant larvae functions redundantly with PAR-2 to maintain polarity in the early embryo. *Development* **137**, 3995-4004 (2010).
28. Hoege, C. *et al.* LGL can partition the cortex of one-cell Caenorhabditis elegans embryos into two domains. *Curr Biol* **20**, 1296-1303 (2010).
29. Hao, Y., Boyd, L. & Seydoux, G. Stabilization of cell polarity by the C. elegans RING protein PAR-2. *Dev Cell* **10**, 199-208 (2006).
30. Schonegg, S., Constantinescu, A.T., Hoege, C. & Hyman, A.A. The Rho GTPase-activating proteins RGA-3 and RGA-4 are required to set the initial size of PAR domains in Caenorhabditis elegans one-cell embryos. *Proc Natl Acad Sci U S A* **104**, 14976-14981 (2007).
31. Schmutz, C., Stevens, J. & Spang, A. Functions of the novel RhoGAP proteins RGA-3 and RGA-4 in the germ line and in the early embryo of C. elegans. *Development* **134**, 3495-3505 (2007).
32. Gotta, M., Dong, Y., Peterson, Y.K., Lanier, S.M. & Ahringer, J. Asymmetrically distributed C. elegans homologs of AGS3/PINS control spindle position in the early embryo. *Curr Biol* **13**, 1029-1037 (2003).
33. Srinivasan, D.G., Fisk, R.M., Xu, H. & van den Heuvel, S. A complex of LIN-5 and GPR proteins regulates G protein signaling and spindle function in C elegans. *Genes Dev* **17**, 1225-1239 (2003).
34. Kumfer, K.T. *et al.* CGEF-1 and CHIN-1 regulate CDC-42 activity during asymmetric division in the Caenorhabditis elegans embryo. *Mol Biol Cell* **21**, 266-277 (2010).
35. Gotta, M., Abraham, M.C. & Ahringer, J. CDC-42 controls early cell polarity and spindle orientation in C. elegans. *Curr Biol* **11**, 482-488 (2001).
36. Schonegg, S. & Hyman, A.A. CDC-42 and RHO-1 coordinate acto-myosin contractility and PAR protein localization during polarity establishment in C. elegans embryos. *Development* **133**, 3507-3516 (2006).
37. Gotta, M. & Ahringer, J. Distinct roles for Galpha and Gbetagamma in regulating spindle position and orientation in Caenorhabditis elegans embryos. *Nat Cell Biol* **3**, 297-300 (2001).
38. Hung, T.J. & Kemphues, K.J. PAR-6 is a conserved PDZ domain-containing protein that colocalizes with PAR-3 in Caenorhabditis elegans embryos. *Development* **126**, 127-135 (1999).

39. Galli, M. *et al.* aPKC phosphorylates NuMA-related LIN-5 to position the mitotic spindle during asymmetric division. *Nat Cell Biol* **13**, 1132-1138 (2011).
40. Panbianco, C. *et al.* A casein kinase 1 and PAR proteins regulate asymmetry of a PIP(2) synthesis enzyme for asymmetric spindle positioning. *Dev Cell* **15**, 198-208 (2008).
41. Shelton, C.A., Carter, J.C., Ellis, G.C. & Bowerman, B. The nonmuscle myosin regulatory light chain gene mlc-4 is required for cytokinesis, anterior-posterior polarity, and body morphology during Caenorhabditis elegans embryogenesis. *J Cell Biol* **146**, 439-451 (1999).
42. Morton, D.G. *et al.* The Caenorhabditis elegans par-5 gene encodes a 14-3-3 protein required for cellular asymmetry in the early embryo. *Dev Biol* **241**, 47-58 (2002).
43. Boyd, L., Guo, S., Levitan, D., Stinchcomb, D.T. & Kemphues, K.J. PAR-2 is asymmetrically distributed and promotes association of P granules and PAR-1 with the cortex in C. elegans embryos. *Development* **122**, 3075-3084 (1996).
44. Colombo, K. *et al.* Translation of polarity cues into asymmetric spindle positioning in Caenorhabditis elegans embryos. *Science* **300**, 1957-1961 (2003).
45. Willis, J.H., Munro, E., Lyczak, R. & Bowerman, B. Conditional dominant mutations in the Caenorhabditis elegans gene act-2 identify cytoplasmic and muscle roles for a redundant actin isoform. *Mol Biol Cell* **17**, 1051-1064 (2006).
46. Liu, J., Maduzia, L.L., Shirayama, M. & Mello, C.C. NMY-2 maintains cellular asymmetry and cell boundaries, and promotes a SRC-dependent asymmetric cell division. *Dev Biol* **339**, 366-373 (2010).
47. Kemphues, K.J., Priess, J.R., Morton, D.G. & Cheng, N.S. Identification of genes required for cytoplasmic localization in early C. elegans embryos. *Cell* **52**, 311-320 (1988).
48. Morton, D.G., Roos, J.M. & Kemphues, K.J. par-4, a gene required for cytoplasmic localization and determination of specific cell types in Caenorhabditis elegans embryogenesis. *Genetics* **130**, 771-790 (1992).
49. Bergmann, D.C. *et al.* Embryonic handedness choice in C. elegans involves the Galpha protein GPA-16. *Development* **130**, 5731-5740 (2003).
50. Lorson, M.A., Horvitz, H.R. & van den Heuvel, S. LIN-5 is a novel component of the spindle apparatus required for chromosome segregation and cleavage plane specification in Caenorhabditis elegans. *J Cell Biol* **148**, 73-86 (2000).
51. Miller, K.G. *et al.* A genetic selection for Caenorhabditis elegans synaptic transmission mutants. *Proc Natl Acad Sci U S A* **93**, 12593-12598 (1996).
52. Wright, A.J. & Hunter, C.P. Mutations in a beta-tubulin disrupt spindle orientation and microtubule dynamics in the early Caenorhabditis elegans embryo. *Mol Biol Cell* **14**, 4512-4525 (2003).
53. Wood, W.B. *et al.* Parental effects and phenotypic characterization of mutations that affect early development in Caenorhabditis elegans. *Dev Biol* **74**, 446-469 (1980).
54. Miwa, J., Schierenberg, E., Miwa, S. & von Ehrenstein, G. Genetics and mode of expression of temperature-sensitive mutations arresting embryonic development in Caenorhabditis elegans. *Dev Biol* **76**, 160-174 (1980).
55. Kodoyianni, V., Maine, E.M. & Kimble, J. Molecular basis of loss-of-function mutations in the glp-1 gene of Caenorhabditis elegans. *Mol Biol Cell* **3**, 1199-1213 (1992).
56. Meneely, P.M. & Herman, R.K. Lethals, steriles and deficiencies in a region of the X chromosome of Caenorhabditis elegans. *Genetics* **92**, 99-115 (1979).
57. Meneghini, M.D. *et al.* MAP kinase and Wnt pathways converge to downregulate an HMG-domain repressor in Caenorhabditis elegans. *Nature* **399**, 793-797 (1999).
58. Rappleye, C.A., Tagawa, A., Lyczak, R., Bowerman, B. & Aroian, R.V. The anaphase-promoting complex and separin are required for embryonic anterior-posterior axis formation. *Dev Cell* **2**, 195-206 (2002).
59. Rose, L.S., Lamb, M.L., Hird, S.N. & Kemphues, K.J. Pseudocleavage is dispensable for polarity and development in C. elegans embryos. *Dev Biol* **168**, 479-489 (1995).
60. Dong, Y., Bogdanova, A., Habermann, B., Zachariae, W. & Ahringer, J. Identification of the C. elegans anaphase promoting complex subunit Cdc26 by phenotypic profiling and functional rescue in yeast. *BMC Dev Biol* **7**, 19 (2007).
61. Guo, S. & Kemphues, K.J. A non-muscle myosin required for embryonic polarity in Caenorhabditis elegans. *Nature* **382**, 455-458 (1996).